

Unlocking HST’s Stellar Treasure Trove: Stellar Activity Minima for HAT-P-11 Offer Prime Windows for Transmission Spectroscopy

PRAJWAL NIRLA ^{1,2} BENJAMIN V. RACKHAM ^{1,2} JULIEN DE WIT ¹ DANIEL APAI ^{3,4,5} MARK S. GIAMPAPA ^{3,4}
DAVID BERARDO ^{1,2} AND CHIA-LUNG LIN ³

¹*Department of Earth, Atmospheric and Planetary Sciences, Massachusetts Institute of Technology, Cambridge, MA 02139, USA*

²*Kavli Institute for Astrophysics and Space Research, Massachusetts Institute of Technology, Cambridge, MA 02139, USA*

³*Department of Astronomy and Steward Observatory, The University of Arizona, 933 North Cherry Avenue, Tucson, AZ 85721, USA*

⁴*Lunar and Planetary Laboratory, The University of Arizona, Tucson, AZ, USA*

⁵*James C. Wyant College of Optical Sciences, The University of Arizona, AZ 85721, USA*

ABSTRACT

HAT-P-11 is a well-studied, active K dwarf hosting an eccentric, misaligned transiting sub-Neptune. As part of the HST Stellar Treasure Trove program (HST-AR-17551), we analyze absolutely calibrated out-of-transit HST spectra from STIS and WFC3 across the G430L, G750L, G102, and G141 bandpasses to constrain the surface heterogeneity of HAT-P-11 and its impact on transmission spectroscopy. Grid-based spectral retrievals using NewEra PHOENIX models robustly favor two-component photospheres in the WFC3 G102 and G141 data, with a ~ 4950 K photospheric component and a cooler (~ 3400 K) component covering 26–33% of the stellar disk. By contrast, retrievals on the STIS optical spectra do not yield a satisfactory fit, reflecting current limitations of stellar atmosphere models in the optical regime compared to the HST observational precision. We contextualize these results using long-term photometric monitoring and chromospheric activity indices. The inferred high spot covering fractions are broadly consistent with the elevated photometric variability observed during the *Kepler* era ($f_{\text{spot}} \sim 10\text{--}20\%$) but are in tension with the much lower rotational amplitudes observed from TESS in the mid 2020s ($f_{\text{spot}} \sim 1\text{--}10\%$). This secular decline in variability is mirrored by a $\sim 20\%$ decrease in the Ca II H&K index. These results imply that HAT-P-11 undergoes comparatively quiescent phases that offer more favorable windows for atmospheric characterization, which serendipitously coincided with some of the recent JWST observations. More generally, our study demonstrates that multi-epoch, space-based stellar spectra provides a physically grounded pathway for mitigating stellar contamination in high-precision transmission spectra in the JWST era.

Keywords: Exoplanet atmospheres (487); Starspots (1572); Stellar Activity (1580)

1. INTRODUCTION

Stellar photospheric heterogeneity is a major challenge in the interpretation of exoplanet transmission spectra. Unocculted starspots and faculae alter the depth of planetary transits, imprinting spectroscopic signals in transmission spectra that bias inferences of planetary atmospheric properties (Pont et al. 2008; Sing et al. 2011; McCullough et al. 2014; Rackham et al. 2017, 2023; Pinhas et al. 2018; Espinoza et al. 2019; Iyer & Line 2020). These effects are significant for late-type and/or active stars, where typical levels of heterogeneity can mimic or mask planetary signals (Rackham et al. 2018, 2019). With the increasing precision of modern observations, correcting for stellar contamination has become the key bottleneck in atmospheric characterization (e.g.,

Lim et al. 2023; Moran et al. 2023; Rackham et al. 2023; Rackham & de Wit 2024; Radica et al. 2025; Rathcke et al. 2025). However, despite growing awareness of this issue, systematic efforts to characterize the surface heterogeneity of exoplanet host stars remain limited.

The Hubble Space Telescope (HST) Stellar Treasure Trove program⁶ (HST AR 17551; PI: Rackham) is an initiative to systematically analyze archival HST transit observations to characterize the surface heterogeneities of exoplanet host stars and quantify their impact on transmission spectra. This program is targeting a sample of exoplanet host stars spanning spectral types from

⁶ <https://hst-stt.github.io/>

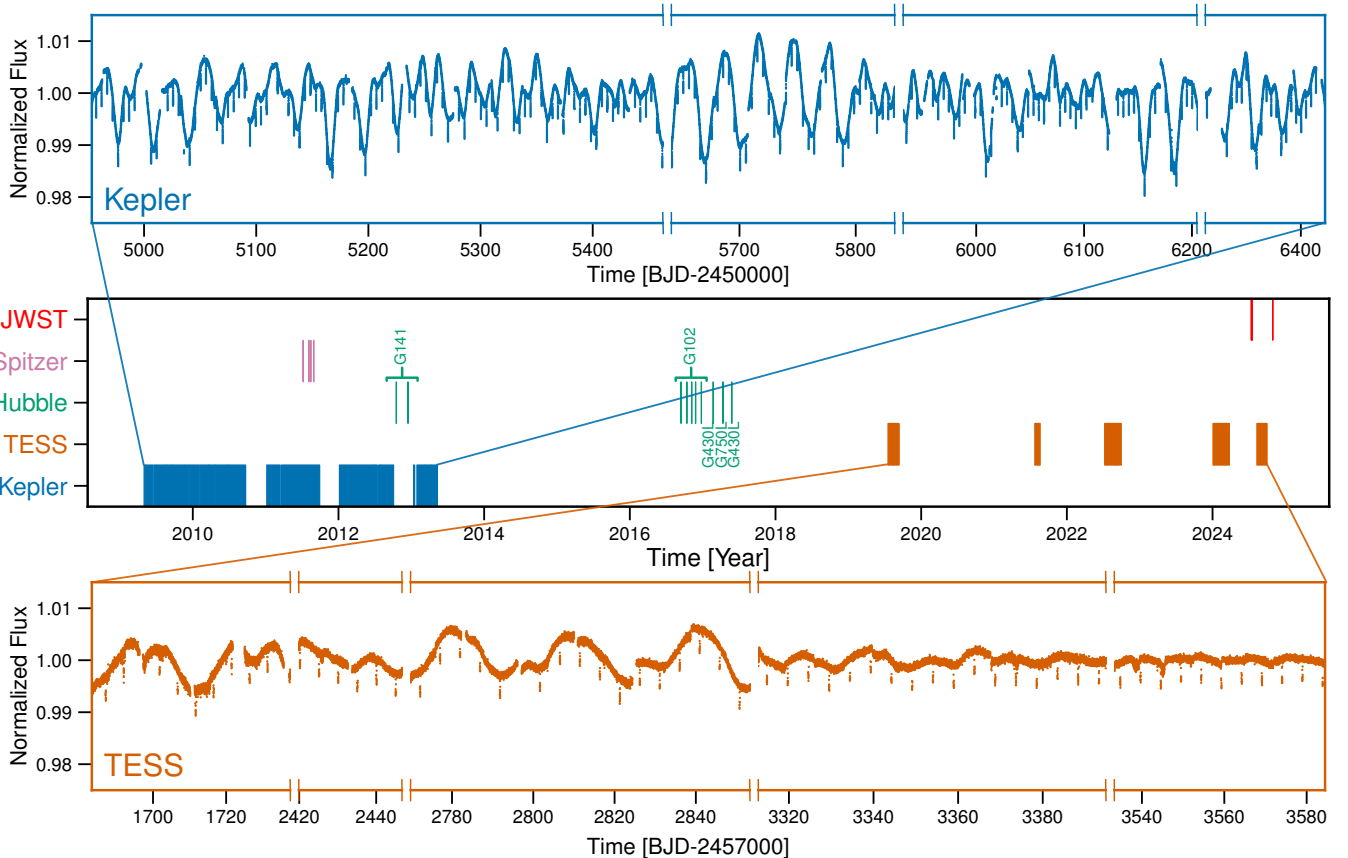


Figure 1. Summary of selected space-based observations of HAT-P-11. **Top:** Four years of Kepler short-cadence photometry showing pronounced rotational modulation and numerous spot-crossing events. **Middle:** Observation timeline for five facilities—Kepler, TESS, HST, *Spitzer*, and JWST—spanning optical to infrared wavelengths. **Bottom:** The TESS light curve, displayed on the same normalized-flux scale as the Kepler data for direct comparison. The rotational modulation amplitude in *TESS* is smaller than in Kepler. The high-cadence data are binned to highlight the modulation signal. The rotational periods inferred from both datasets are consistent with the previously reported value of 29.2 ± 0.5 days.

F to late M, covering a broad range of stellar temperatures, metallicities, and activity levels. A pilot analysis of HD 189733 (Narrett et al. 2024) (henceforth N24) demonstrated that stellar component temperatures and covering fractions can be robustly extracted from HST WFC3/G141 spectra. These spectral inferences point to larger spot filling factors than previously estimated for this active K dwarf, motivating the extension of this approach to other active planet-hosting stars of high interest for transmission spectroscopy.

Among such compelling targets is the HAT-P-11 system. With a favorable brightness ($V = 9.5$), HAT-P-11 is a chromospherically active K4 dwarf ($\log R'_{HK} \approx -4.35$) hosting a misaligned transiting Neptune-sized planet, HAT-P-11 b, on a short-period (4.88 d), eccentric ($e \approx 0.26$) orbit (Bakos et al. 2010; Sanchis-Ojeda & Winn 2011; Morris et al. 2017a). Early transmission spectroscopy efforts reported water absorption in the atmosphere of HAT-P-11 b (Fraine et al. 2014), later confirmed with additional HST observa-

tions (Chachan et al. 2019; Cubillos et al. 2022). More recent high-resolution ground-based spectroscopy independently supports these detections, reporting additional molecular signatures of NH_3 and CO_2 (Basili-cata et al. 2024). Helium absorption from the planet’s extended exosphere has also been detected (Mansfield et al. 2018).

Interpreting these signals, however, is complicated by the star’s active and variable surface. HAT-P-11’s spots are unusually well characterized, given the fortuitous combination of the planet’s high obliquity and four years of high-precision Kepler photometry showing multiple clear spot crossings. While previous analyses have focused on in-transit data—including spot-crossing anomalies (Morris et al. 2017a) and the planetary transmission spectrum (Fraine et al. 2014; Chachan et al. 2019)—to understand the spottedness of HAT-P-11 and its impact on observations of the planetary atmosphere, none has systematically probed what can be gleaned from the out-of-transit spectra themselves.

Here we leverage the extensive database of HST stellar spectra to directly constrain the disk-integrated photospheric heterogeneity of HAT-P-11 and evaluate its implications for transmission spectroscopy. We develop a robust framework for characterizing stellar heterogeneity in multi-epoch, multi-instrument HST datasets. We place our results in context by comparing them to independent estimates of spot properties derived from photometric monitoring (Rackham et al. 2019), spot-crossing analyses (Morris et al. 2017a), molecular band modeling (Morris et al. 2019) and chromospheric activity estimates (Morris et al. 2017b, 2025; Yee et al. 2018) spanning more than a decade of observations.

This paper is organized as follows. In Section 2, we describe the multi-epoch and multi-instrument HST observations, including our reduction framework to extract these spectra, and complementary datasets used in our analysis. In Section 3, we present our stellar modeling and parameter fitting framework. We summarize the results of our spectral analysis in Section 4, including constraints on spot temperatures, filling factors, and temporal variability. In Section 5, we contextualize our results using Kepler and TESS photometric data and chromospheric activity indicators for HAT-P-11, and compare them with previous studies of this system and other active K dwarfs. The implications of the stellar contamination are discussed in detail in Section 6. Finally, we summarize our main conclusions in Section 7.

2. OBSERVATIONS AND DATA REDUCTION

Discovered via a ground-based transit survey (Bakos et al. 2010), HAT-P-11 has since been observed extensively with both space- and ground-based facilities, including HST, *Spitzer*, and JWST (see Figure 1). In this work, we focus on the rich archive of HST spectroscopy. Here, we outline our methodology for extracting stellar spectra from these observations and summarize the additional datasets used in our analysis.

2.1. HST Spectroscopy

HAT-P-11 has been observed with HST over multiple epochs using different instruments and grisms. These observations span 0.3–1.7 μm using STIS and WFC3, each with two dispersers, as listed in Table 1. A key advantage of HST is its well-calibrated response function, which enables precise and accurate absolutely calibrated flux measurements (e.g., Wakeford et al. 2019; Garcia et al. 2022; N24). For each disperser, we conservatively restrict the wavelength range to exclude the edges of the transmissivity curve (see Table 1). In the following, we describe the data reduction procedures employed for each instrument.

2.1.1. WFC3 G102 and G141 Observations

HST observed HAT-P-11 twice with WFC3/G141. One visit (2012-12-15) is excluded from both previous analyses (Chachan et al. 2019) and our analysis due to pronounced systematics. Additionally, five WFC3/G102 visits occurred over the course of three months in 2016, all of which are included in our analysis. Together, these data span a wavelength range of 0.8–1.6 μm and have a spectral resolving power of $R \sim 100\text{--}200$.

We extracted spectra for both G102 and G141 grisms using the PACMAN pipeline (Zieba & Kreidberg 2022). Our procedure closely follows the methodology of N24. The reduction yields a spectroscopic time series in terms of photon counts following background subtraction, dark correction, and cosmic ray corrections. To convert these into absolutely calibrated fluxes, we use the HST sensitivity curves⁷ and account for the stellar radius and distance as well as the instrumental resolution and exposure time.

Spectral extraction with PACMAN employs both box summation and optimal extraction techniques. In typical fashion, PACMAN calibrates wavelength by the source position in the direct image. When extracting the spectra, telescope pointing drift can introduce minor errors in the wavelength calibration solution. In WFC3, each pixel corresponds to $\sim 25 \text{ \AA}$, so small shifts of a few pixels may influence the wavelength calibration, though they typically do not exceed $\sim 100 \text{ \AA}$. To mitigate this, we applied a post-processing step to correct the wavelength calibration by comparing the observed photon counts with the expected flux count from a PHOENIX NewEra model (Hauschildt et al. 2025). This wavelength adjustment is performed at the count level, prior to the absolute flux conversion, which involves division by the wavelength-dependent sensitivity curve.

WFC3 time-series data are also affected by charge trapping, which produces ramp-like systematics in the light curves (Zhou et al. 2017). We model these effects using a parametric double-exponential model (de Wit et al. 2018), which we then use to normalize the spectroscopic time series. The stellar spectra are extracted by computing the median of the out-of-transit exposures after masking the in-transit data. Uncertainties are estimated from the scatter in the spectroscopic time series and are generally larger than the formal Poisson noise. When combining multi-epoch observations for each instrument, the spectra are supersampled and interpolated onto a common wavelength grid, with uncertainties re-estimated from the scatter.

⁷ G102 Sensitivity Curve & G141 Sensitivity Curve

Table 1. *Hubble* Observations of HAT-P-11

Date	Instrument	Disperser	Proposal ID	PI	Bandpass [\AA]	Exposures	Orbits	Exp. Time [s]	Reference
2012-10-18	WFC3	G141	12449	D. Deming	11450–16575	113	4	44.357	F14
2016-09-14	WFC3	G102	14793	J. Bean	8100–11350	99	4	81.089	M18
2016-10-13	WFC3	G102	14793	J. Bean	8100–11350	99	4	81.089	M18
2016-11-07	WFC3	G102	14793	J. Bean	8100–11350	99	4	81.089	M18
2016-11-26	WFC3	G102	14793	J. Bean	8100–11350	99	4	81.089	M18
2016-12-26	WFC3	G102	14793	J. Bean	8100–11350	99	4	81.089	M18
2017-02-22	STIS	G430L	14767	D. Sing	3224–5678	82	5	140.0	Y19
2017-04-12	STIS	G750L	14767	D. Sing	5305–10153	81	5	140.0	Y19
2017-05-26	STIS	G430L	14767	D. Sing	3224–5678	81	5	140.0	Y19

NOTE—F14 – Fraine et al. (2014); M18 – Mansfield et al. (2018); Y19 – Chachan et al. (2019).

Table 2. System Properties of HAT-P-11

Property	Units	Value	Reference
TIC Identifier	-	28230919	S19
T_{eff}	K	4778^{+118}_{-107}	M17
Fe/H	dex	0.31 ± 0.05	B10
M	M_{\odot}	$0.770^{+0.100}_{-0.076}$	B10
R	R_{\odot}	$0.760^{+0.045}_{-0.051}$	B10
ρ	gm/cm^3	$2.474^{+0.641}_{-0.590}$	B10
$\log g$	gm/cm^3	$4.563^{+0.093}_{-0.081}$	S19
Parallax	arcsec	7.044 ± 0.010	G23
Distance	pc	141.965 ± 0.201	G23
Rotation Period	days	29.2	S11
Spin-Orbital [Ψ]	deg	106^{+15}_{-11}	S11
Photometric Values			
B		10.556 ± 0.141	S19
V		9.46 ± 0.03	S19
J (2 MASS)		7.608 ± 0.029	S06
H (2 MASS)		7.131 ± 0.021	S06
K (2 MASS)		7.009 ± 0.020	S06

NOTE— S19 – Stassun et al. (2019) | M17 – Morris et al. (2017a) | B10 – Bakos et al. (2010) | G23 – Gaia Collaboration et al. (2023) | S11 – Sanchis-Ojeda & Winn (2011) | S06 – Skrutskie et al. (2006)

2.1.2. STIS G430L and G750L Observations

STIS observations of HAT-P-11 were obtained using the G430L and G750L gratings. Two visits were gathered with G430L and one with G750L. Together, these data span a wavelength range of 0.30–1.03 μm and have a spectral resolving power of $R \sim 500$ –1000. We processed all STIS observations using the CALSTIS pipeline,

which produces 1D flux-calibrated spectra for each orbit. The pipeline applies standard flat-fielding, wavelength calibration, and cosmic ray rejection steps. The G750L data show pronounced fringing at wavelengths $>7000 \text{\AA}$. We mitigated this using contemporaneous flat field exposures and the DEFRINGE functionality within CALSTIS (Goudfrooij & Christensen 1998).

Uncertainties are typically on the order of 1%, estimated from visit-to-visit scatter whenever possible. Additional systematics may arise from several sources, including the instrument’s sensitivity drift, detector effects, and persistence. To evaluate if such effects impact our dataset, we compare overlapping wavelength regions among G430L, G750L, and G102 observations (see Figure 2). Once the fluxes are appropriately scaled (which does not affect our astrophysical inferences, as shown in N24), and the resolution is matched, the continua among G430L, G750L, and G102 agree within $\sim 1\%$, demonstrating that our typical uncertainties of 2% adequately capture the typical noise sources.

2.2. Supporting Data Sets

2.2.1. Photometry

In addition to the HST spectra, we incorporate calibrated broadband SED measurements in B and V bands (Stassun et al. 2019) as well as 2MASS J , K & H bands (Skrutskie et al. 2006), together with the Gaia DR3 parallax (Table 2). These measurements anchor the absolute stellar flux and provide additional constraints on global stellar parameters. Since these broadband data are well calibrated, we include them alongside the HST spectra in our analysis without inflating their uncertainties or introducing vertical offsets.

Similarly, photometric timeseries probe stellar activity by showing the changes in the emergent surface flux (Shapiro et al. 2017). HAT-P-11 benefits particularly

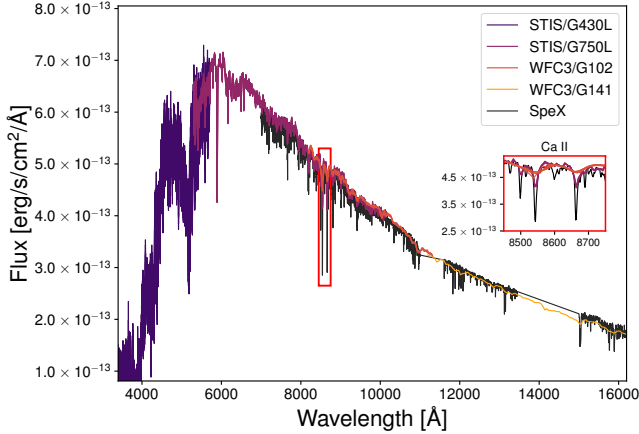


Figure 2. Optical and near-infrared spectra of HAT-P-11. The HST spectra of HAT-P-11 were obtained with STIS (G430L, two visits; G750L, one visit) and WFC3 (G102, five visits; G141, one visit), spanning 0.3–1.7 μm . We show these data alongside an IRTF/SpeX spectrum ($R \sim 2000$ of HAT-P-11, which better resolves the Ca II infrared triplet. The Ca II region is highlighted in the main panel and shown in the inset to illustrate the effect of spectral resolution in G750L, G102, and SpeX data. All spectra are vertically scaled to match the STIS/G750L continuum level. After accounting for differences in resolution and wavelength sampling, the spectra from the various HST modes are consistent at the 1–2% level.

from extensive and precise long-term space-based photometry from Kepler (Borucki et al. 2010) and TESS (Ricker et al. 2015). Kepler observed HAT-P-11 in short cadence mode for roughly 4 years from 2009 to 2013, while TESS observed it across 11 sectors, which includes fast cadence mode of 20 seconds for the last 9 sectors (see Figure 1).

2.2.2. IRTF/SpeX

We observed HAT-P-11 on 21 Jul 2025 with the SpeX spectrograph (Rayner et al. 2003) on the 3.2-m NASA Infrared Telescope Facility (IRTF). Spectra were gathered using the short-wavelength cross-dispersed (SXD) mode and the $0''.3 \times 15''$ slit aligned to the parallactic angle, yielding 0.70–2.42 μm coverage with a spectral resolving power of $R \sim 2000$. Conditions were clear with seeing of $0''.7$. We collected six 60-s exposures in an AB-BAB nodding pattern at an airmass of 1.2, followed by the standard SXD calibration sequence and observations of an A0 V standard at a similar airmass. The data were reduced using Spextool V4.1 (Cushing et al. 2004) with standard settings (e.g., Delrez et al. 2022; Barkaoui et al. 2023; Ghachoui et al. 2023). The final reduced spectrum has a median S/N of 400 per resolution element.

3. STELLAR SPECTRAL MODELING

In this section, we describe our framework for modeling the disk-integrated stellar spectrum of HAT-P-11. We outline our parameterization of photospheric heterogeneity along with the adopted stellar atmosphere models, and our prior choices. We then detail our fitting procedure, including a description of the likelihood function and inference methodology.

3.1. Stellar Heterogeneity Model

The visible heterogeneous stellar surface can be represented as a linear combination of distinct spectral surface components, such as the quiet photosphere, cool spots, and hot faculae. In this work, we model the disk-integrated stellar flux as the sum of spectra from N components with different effective temperatures:

$$F = \sum_{i=1}^N f_i F_i, \quad (1)$$

where F_i is the model spectrum of the i^{th} component and f_i is its fractional coverage of the projected stellar disk (i.e., filling factor), subject to the normalization condition $\sum_i^N f_i = 1$. All components are assumed to share $\log g$ and metallicity, differing only in effective temperature.

In this framework, discrepancies between observed spectra and a single-component model are interpreted as unresolved surface heterogeneity. We explore models with up to four surface components, each characterized by an independent temperature and covering fraction. We note that even when a single-component model is statistically preferred, multi-component fits remain informative. In particular, two-component models provide an upper bound on the total spottedness compatible with the data, quantifying how much heterogeneous surface coverage can be tolerated before the model becomes inconsistent with observations.

Following N24, we impose an ordering condition on the filling factors to prevent label degeneracies,

$$f_1 > f_2 > \dots > f_N, \quad (2)$$

and adopt a Dirichlet prior to enforce the normalization constraint. While this prior does not directly constrain the component temperatures, we typically expect the dominant component (F_1 , parameterized by T_1 and f_1) to correspond to the quiescent photosphere, with additional components representing cooler spots and/or hotter faculae at smaller filling factors. Models with up to four components are physically motivated by the expected presence of quiescent photosphere, umbra, penumbra, and faculae. For a more detailed discussion of this framework, please see Section 3 of N24.

3.2. Stellar Atmosphere Models

For our spectral fitting, we adopt the PHOENIX New-Era stellar atmosphere models (Hauschildt et al. 2025). This grid spans a wide range of effective temperatures (sampled at ~ 100 K intervals) and metallicities up to $+0.5$ dex, with $\log g$ sampled in 0.5 dex steps. Model access and interpolation are handled through the `speclib` toolkit⁸ (Rackham 2023; Rackham & de Wit 2024), which enables bilinear interpolation in effective temperature, $\log g$, and metallicity to generate spectra at arbitrary parameter values.

We adopt the PHOENIX NewEra model grid uniformly across all datasets to ensure consistency. While specialized starspot atmosphere models would be desirable (e.g., Smitha et al. 2025), PHOENIX provides the broad wavelength and parameter coverage required for our analysis. Our framework is readily extensible to future spot spectral model grids as they become available.

3.3. Parameterization and Prior Choices

The literature values we adopt for stellar parameters are listed in Table 2. We impose Gaussian priors on the stellar distance and radius and a truncated normal distribution on metallicity (Fe/H) centered on the value reported by Bakos et al. (2010), with the truncation set by the limits of the stellar model grid. Because surface gravity is only weakly constrained by our low-resolution spectra, we adopt a fixed value of $\log g = 4.563$ from Stassun et al. (2019).

The stellar distance and radius enter the model as multiplicative flux scalings. For HST spectra, we additionally allow for an independent instrument-specific scaling factor to account for small systematic offsets (e.g., forward vs. reverse spatial scans; N24). Absolutely calibrated broad photometry is not assigned such a scaling term, thus providing an anchor for the HST fluxes.

To ensure consistency across instruments, model spectra are sampled on a uniform 1 \AA wavelength grid, sufficient to resolve the instrumental line-spread function. We empirically determine and fix the effective convolution kernel for each instrument using a broad sample of stellar spectra from the HST Stellar Treasure Trove program. Given that the instrumental resolution is stable across visits, fixing these kernels reduces computational overhead.

3.3.1. Single-Mode Fitting

HAT-P-11 exhibits variability on both rotational (29.2 d) and multi-year magnetic-cycle timescales, as

traced by the \mathcal{R}'_{HK} index (Morris et al. 2017b). Different observing epochs therefore likely sample distinct activity states.

We began by fitting each epoch independently, starting with the five G102 visits obtained over three months. These spectra include prominent Ca II infrared triplet lines, which serve as diagnostics of the star’s activity. Given the stellar rotation period, these visits probe different rotational phases and thus potentially different spot configurations and covering fractions.

We then performed a fit where we combined all available epochs for a given disperser to increase the signal-to-noise ratio. While stacking increases precision, intrinsically time-variable regions (e.g., the Ca II triplet; Figure 2) show increased scatter and are therefore down-weighted in the fit. This fit enables us to constrain persistent levels of the spottedness across epochs.

3.3.2. Multi-Mode Fitting

Fits to single instrumental modes are susceptible to degeneracies, as models of differing complexity can reproduce limited spectral regions equally well. However, when extrapolated to broader wavelength coverage—particularly into the optical—the predictions from single- and multi-component models diverge substantially. This motivates simultaneous fitting across all available instrument modes.

A complication is that the multi-instrument dataset spans multiple epochs during which HAT-P-11 likely exhibited varying activity levels. Consequently, the combined fit should be interpreted as providing an effective, time-averaged description of the stellar surface rather than a snapshot of a single activity state.

In the joint retrieval, we allow for independent flux-scaling and error-inflation terms for each instrument (Equation 5). When comparing the model to the broadband photometry fluxes, we adopt the mean of the epoch-specific filling factors as an effective, time-averaged description of the stellar surface. We also tested fits that allowed filling factors to vary between instruments while fitting for a consistent spot temperature.

3.4. Likelihood Function and Inference Method

We perform parameter estimation using dynamic nested sampling as implemented in DYNESTY (Speagle 2020). The sampler is initialized with 1000 live points, using the `rslice` method with bounding method set to `multis` to efficiently explore the posterior distribution. The maximum number of iterations was set to 500,000 to ensure convergence and adequate exploration of degenerate regions of parameter space.

⁸ <https://github.com/brackham/speclib>

To account for unmodeled systematics or underestimated uncertainties, we introduce an error-inflation (“jitter”) term in the likelihood function. The log-likelihood is given by:

$$\ln \mathcal{L} = -\frac{1}{2} \sum_{\lambda} \left(\frac{(F_{\text{Obs},\lambda} - F_{\text{Model},\lambda})^2}{\sigma_{\lambda}^2} + \ln(2\pi\sigma_{\lambda}^2) \right) \quad (3)$$

where the total model variance is modeled as:

$$\sigma_{\lambda}^2 = \sigma_{\text{Photon},\lambda}^2 + \sigma_{\text{Jitter},\lambda}^2. \quad (4)$$

Following previous studies (N24; Rackham & de Wit 2024), we parameterize this additional source of error as:

$$\sigma_{\text{Jitter},\lambda} = f_{\text{var}} F_{\text{Model},\lambda} \quad (5)$$

in which f_{var} is a free multiplicative scaling factor that inflates the model-dependent uncertainties, effectively introducing a heteroscedastic noise model in which the variance scales with the model-flux. This formulation provides a parsimonious way to absorb additional uncertainties.

4. RESULTS

Here, we present the major results of our analysis. We first discuss the evidence for photospheric heterogeneity from the out-of-transit spectra of HAT-P-11. We then quantify the inferred spot temperatures and covering fractions, examine their temporal evolution, and finally assess the impact of multi-instrument-mode fitting and data-driven tests of spectral variability.

4.1. Evidence for Surface Heterogeneity

Results from the single-instrument HST spectra retrievals for up to three-component models are summarized in Table 5. Based on Anderson–Darling (AD) statistics (Anderson & Darling 1954), we obtain statistically adequate fits for WFC3 datasets (G102 and G141), but not for the STIS datasets (G430L and G750L). For G430L and G750L, AD values exceed 2, indicating departures from Gaussian residuals, whereas WFC3 datasets yield AD values near or below 1, consistent with Gaussian noise at the 5% level. This mismatch is also reflected in the large error-inflation factor required for G430L and G750L, which is more than two orders of magnitude higher than that of the WFC3 datasets. The G430L retrieval additionally drives the metallicity to the upper prior bound (+0.50), in $<3\sigma$ tension with published estimates. We discuss these discrepancies further in Section 5.1.

Model comparison using the Bayesian Information Criterion (BIC) show that the optical datasets (G430L

and G750L) favor a single-component model, with the ΔBIC value indicating little support for additional complexity. By contrast, both WFC3 datasets (G102 and G141) strongly prefer a two-component model over a single-component model ($\Delta\text{BIC} \sim 15$ for G102 and $\Delta\text{BIC} \sim 22$ for G141). ΔBIC values greater than 10 constitute strong evidence for the more complex model. Three-component models are not supported by the BIC for any dataset. Fits for each instrument mode, modeled up to three components, are shown in Figure 3.

4.2. Spot Temperatures and Covering Fractions

For the combined G102 dataset, we infer a photospheric temperature of $T_1 = 4966^{+33}_{-41}$ K, a spot temperature of $T_2 = 3617^{+125}_{-149}$ K, and a spot filling factor of $f_2 = 0.264^{+0.038}_{-0.043}$. For G141, we obtain $T_1 = 4950^{+32}_{-27}$ K, $T_2 = 3326^{+110}_{-119}$ K, and $f_2 = 0.282^{+0.045}_{-0.051}$. The retrieved photospheric temperatures are consistent between the two bandpasses and exceed literature effective temperature estimates, as would be expected if the literature values were averaging over a highly spotted photosphere. The retrieved spot temperatures differ modestly (1.6σ) between G102 and G141, and both datasets indicate substantial spot coverage at the $\sim 25\text{--}30\%$ level.

Although individual components in multi-component model are degenerate, the composite spectra are tightly constrained (Figure 3), and the consistency between independent WFC3 modes strengthens the case for significant photospheric heterogeneity.

4.3. Temporal Evolution of Spot Properties

Restricting ourselves to the WFC3 results, we next assess epoch-specific fits to assess temporal variability. The G141 visit in late 2012 favors a two-component model with a photospheric temperature of $T_1 = 4950^{+32}_{-27}$ K and a cooler spot component of $T_2 = 3300^{+110}_{-119}$ K, with a filling factor of $f_2 = 28.2^{+4.5}_{-5.1}\%$. Four years later, the five G102 observations in late 2016 similarly favor two-component solutions, with photospheric temperatures clustered near ~ 4950 K and spot temperatures between $\sim 3529\text{--}3647$ K (Figure 4). Across the roughly three-month sequence, the inferred filling factors remain remarkably stable ($\sim 25\text{--}27\%$), suggesting persistent and substantial spot coverage rather than transient spot emergence. The primary variability appears to be modest fluctuations in covering fraction ($1\text{--}2\%$) rather than large changes in spot temperature, validating our approach for the multi-epoch fits.

4.4. Multi-Mode Fits

We again exclude the STIS datasets from the joint fits because the available photospheric models do not

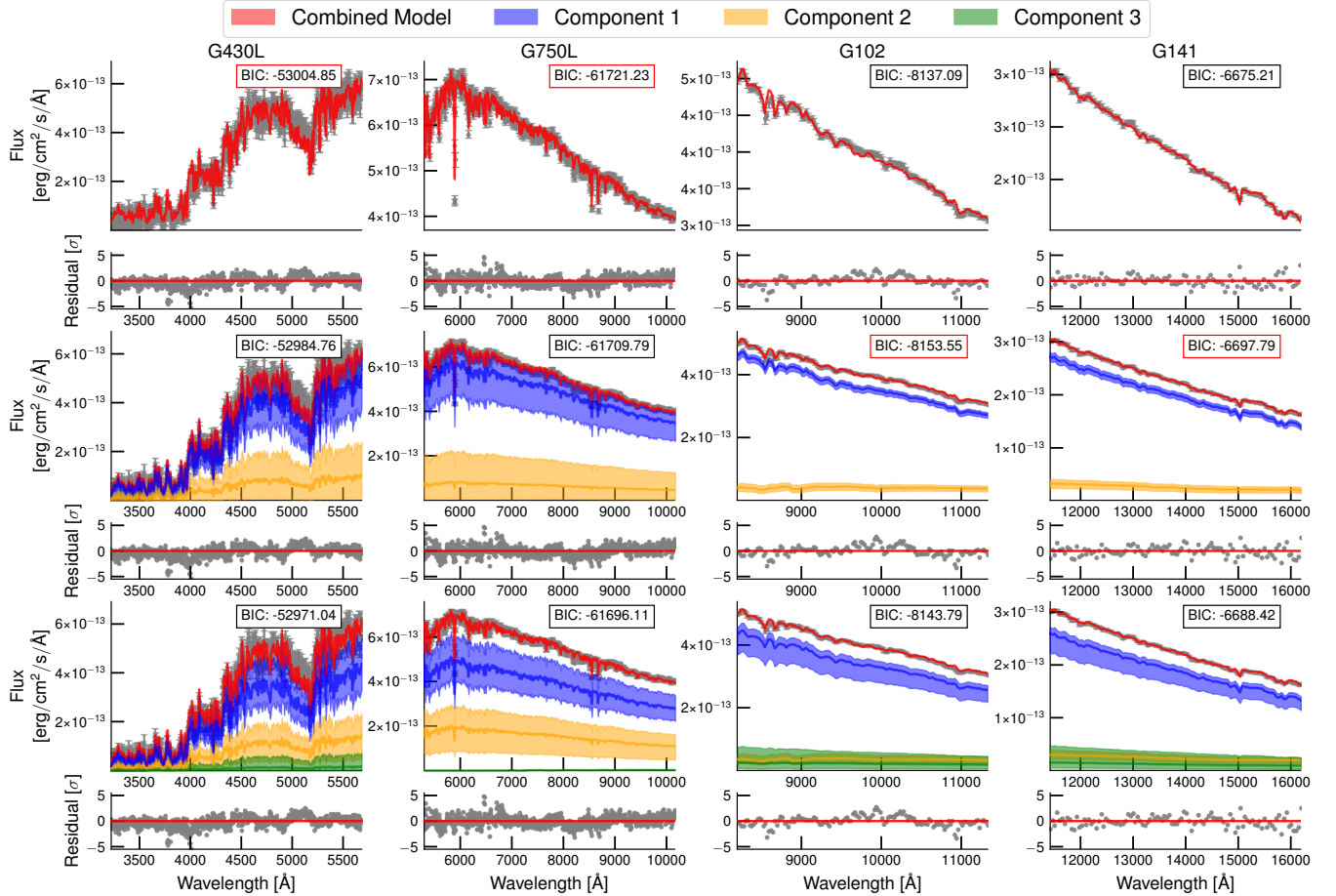


Figure 3. Stellar spectral modeling of HAT-P-11 from blue to red wavelengths (STIS/G430L, STIS/G750L, WFC3/G102, and WFC3/G141). Fits are performed on the averaged spectra for each mode, with uncertainties estimated from the data scatter. In each pair of flux and residual panels, the top panel shows the observed spectrum (gray) and the best-fit combined model (red), with residuals displayed below. The first pair of rows shows the single-component model, the second pair the two-component model, and the third pair the three-component model. Contributions from the individual components are indicated by colored curves (blue, orange, and green), and their sum is shown in red. The Bayesian Information Criterion (BIC) for each fit is shown in the upper panels; the preferred model in each wavelength range is highlighted with a red box.

adequately reproduce those spectral regions and do not yield a reliable spot constraint (see Section 5.1). We therefore perform joint fits using G102 and G141 only, allowing for independent filling factors but a common spot temperature.

The combined analysis strengthens the preference for a two-component model and does not support the addition of a third component. A joint fit to G102+G141, assuming a common spot temperature but independent filling factors, yields tighter constraints: $T_1 = 4979_{-24}^{+20}$ K and $T_2 = 3412_{-73}^{+77}$ K. The inferred filling factors are $f_{2,G102} = 0.259_{-0.023}^{+0.020}$ and $f_{2,G141} = 0.331_{-0.046}^{+0.041}$. As expected, the combined analysis sharpens the spot temperature constraint, with the joint value lying between those obtained from the individual fits. The filling factors are consistent with the individual fits as well, rein-

forcing the inference of a persistent large areal coverage of spots contributing to the integrated disk spectra.

4.5. Data-Driven Spectral Comparison

We additionally tested for intrinsic spectral variability of HAT-P-11 using the five *HST*/WFC3 G102 visits obtained over three months. To maximize sensitivity to potential changes, we compared spectra from the epochs with the highest and lowest median out-of-transit fluxes. For each visit, we computed median out-of-transit fluxes (Figure 5) and identified the brightest and faintest epochs. We then constructed two median spectra by combining the five highest-flux exposures for the brightest epoch and the five lowest-flux exposures for the faintest epoch. This approach suppresses noise and reduces the impact of transient artifacts such as cosmic rays.

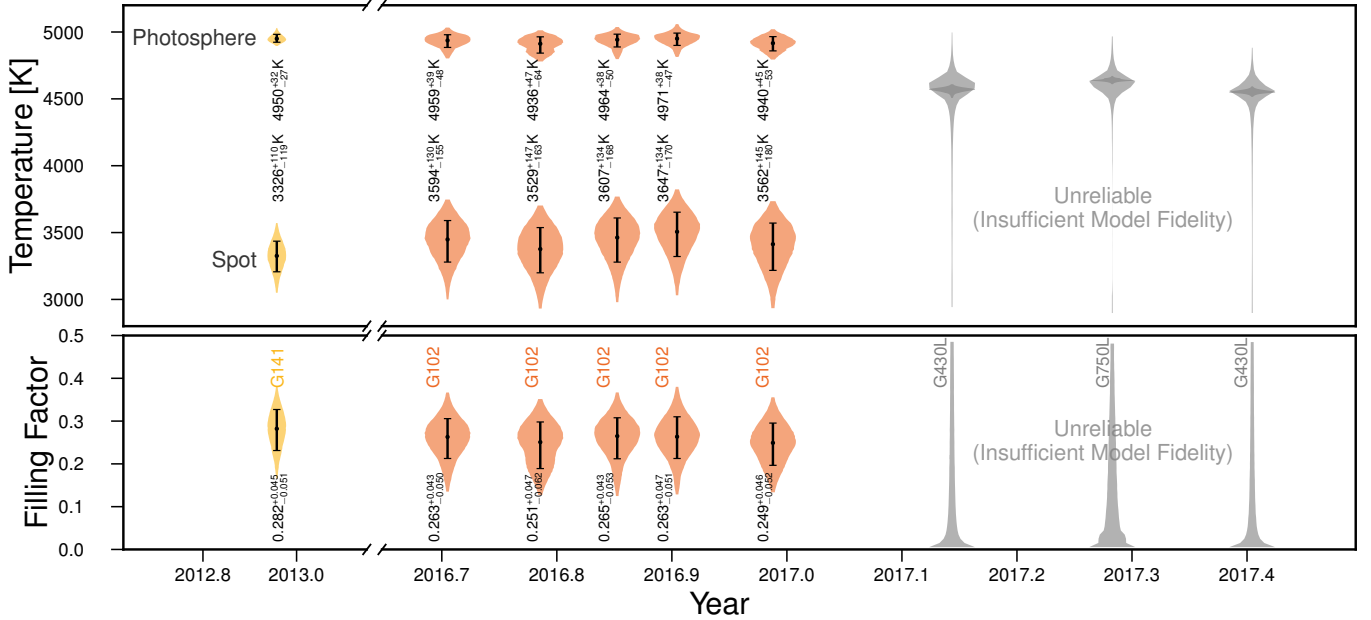


Figure 4. Time series of stellar temperature components and spot filling factor from two-component spectral fits. **Top:** Retrieved values of the photospheric temperature (T_1) and spot temperature (T_2) for each HST epoch. For the STIS datasets (gray), the inferred photosphere and spot temperatures strongly overlap, indicating that the two-component model does not meaningfully separate distinct temperature components; these results are not considered reliable due to significant residuals (see Section 5.1) and are shown for completeness only. **Bottom:** Corresponding inferences of the spot filling factor (f_2) as a function of epoch.

The resulting median spectra are nearly identical in spectral shape across the full G102 bandpass (Figure 5). Although HAT-P-11 exhibits $\sim 1\%$ flux modulation across these visits, no obvious wavelength-dependent structure is apparent at the precision of these data. The variability therefore appears largely achromatic, consistent with changes in surface coverage of features rather than large temperature-driven spectral differences. This interpretation aligns with our epoch-by-epoch retrievals (Section 4.3), which show stable photospheric and spot temperatures and attribute most of the variability to changes in filling factors.

The strongest absorption features in the WFC3 spectra of HAT-P-11 are the strong Ca II infrared triplet absorption features at 8498 Å, 8542 Å, and 8662 Å, well-known diagnostics of stellar activity (Andretta et al. 2005). These lines exhibited the largest apparent visit-to-visit differences (see Figure 2). However, further analysis indicated that much of this variability arose from differences in spectral sampling between visits. The combined Ca II equivalent widths show no significant mutual correlations or correlations with retrieved stellar surface properties within the measurement uncertainties. Similarly, the 2025 SpeX spectrum which covers the Ca II infrared triplet region (Figure 2) at a resolution of ~ 2000 does not show obvious signs of emission features, which sometimes are seen in active stars.

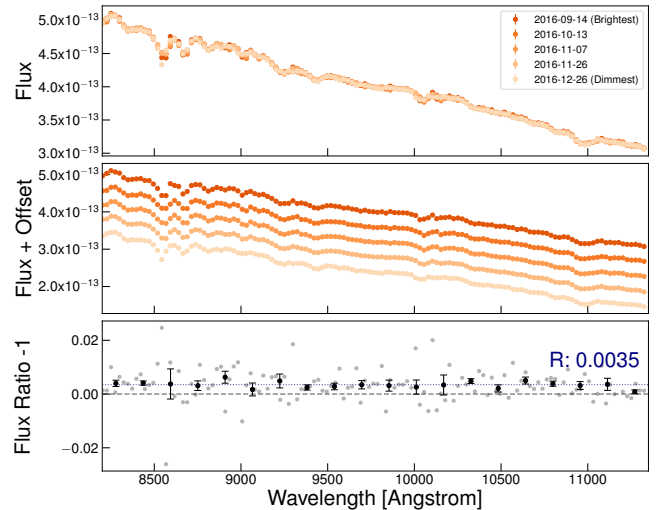


Figure 5. Comparison of five WFC3/G102 spectra obtained at different epochs. **Top:** Extracted stellar flux for each epoch shown without scaling, demonstrating consistency in flux levels and spectral shape. **Middle:** The same spectra, vertically offset for clarity. **Bottom:** The ratio of the brightest epoch to the dimmest. The brightest spectrum is elevated by 0.35% relative to the faintest, with no wavelength-dependent structure. This uniform offset indicates instrumental stability and suggests that the stellar inhomogeneities remain relatively stable across five visits.

5. DISCUSSION

Our results reveal a picture of HAT-P-11 as a highly spotted K dwarf whose near-infrared spectra require multiple components to model. At the same time, the optical STIS spectra do not support multi-component models. Reconciling this discrepancy is essential both for interpreting the stellar surface properties and for assessing how stellar contamination affects the transmission spectrum of HAT-P-11 b. We therefore first examine why STIS disfavors two-component models, then reassess the WFC3 evidence for multi-component photospheres, place our results in the context of previous studies, and investigate other evidence of HAT-P-11’s stellar activity and its long-term evolution.

5.1. Why Do STIS Results Not Favor Two-Component Models?

The STIS spectra show no statistical preference for multi-component photospheric models. This result should be interpreted in the broader context of wavelength-dependent model fidelity and the challenges associated with modeling contamination from cooler photospheric components (Iyer & Line 2020; Rackham & de Wit 2024). Because this work represents one of the first attempts to use wide-bandpass, absolutely calibrated spectra to probe stellar surface inhomogeneities, the inferred spot properties naturally depend on the underlying stellar atmosphere models employed.

To assess how well the PHOENIX NewEra grid models reproduce realistic stellar atmospheres, we compared them against first-principles simulations of active-region spectral components for a K0 dwarf from Smitha et al. (2025), which is the closest available analog to HAT-P-11. In Figure 6, the top panel shows the disk-integrated fluxes for the photosphere, spot, penumbra, and umbra components from the Smitha et al. (2025) model (solid curves) and the corresponding PHOENIX models (dotted curves). Overall, the models reproduce the large-scale continuum shape and the temperature ordering of the components reasonably well, confirming that the grid captures the broad spectral energy distribution (SED) of K dwarfs and their cooler surface components.

However, the residuals reveal wavelength-dependent discrepancies in the models, especially in the optical. The discrepancies are largest in the G430L region (roughly 3000–5700 Å), with secondary tension extending into the G750L region (5500–10000 Å). These tensions are not limited to reproducing spot spectra with PHOENIX models. In fact, the differences between the photospheric models similarly show discrepancies in this wavelength regime exceeding the 2% precision of the STIS data. These deviations arise because the opti-

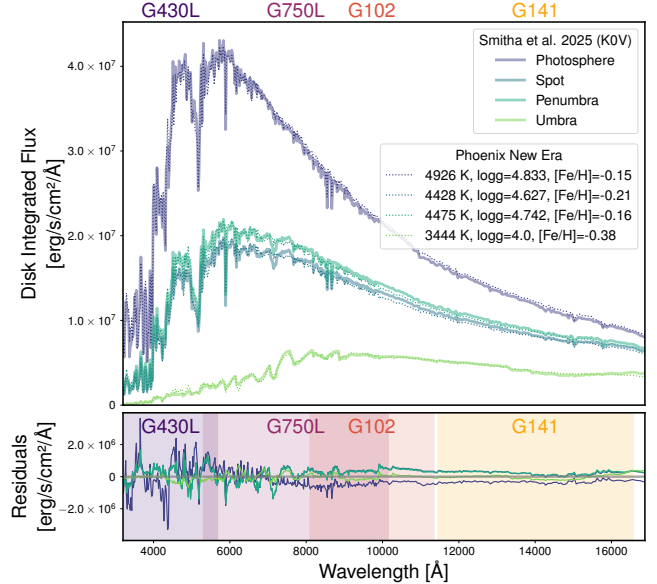


Figure 6. Comparison between the first-principles-based models of Smitha et al. (2025) and the best-fitting one-component stellar model from PHOENIX NewEra grid. **Top:** Disk-integrated flux spectra for the photosphere, spot, penumbra, and umbra components (Smitha et al. 2025, solid lines) alongside the corresponding PHOENIX models (dotted lines). Agreement between models is strongest within the G102 and G141 bands, whereas larger discrepancies arise in the G430L and G750L regions. **Bottom:** Residuals between the two models. The wavelength ranges of the HST dispersers are shaded for reference.

cal regime is dominated by dense atomic and molecular line blanketing, which suppresses the continuum, distorts line depths, and complicates the comparison of the pseudo-continuum between data and models. In addition, uncertain or incomplete line lists and NLTE effects disproportionately affect this regime. Such discrepancies between the model and the data have already been highlighted for M-dwarfs (Iyer et al. 2023, 2025; Wilson et al. 2025, see their Figure 5), and we find that they likely extend to K dwarfs as well.

As a result, STIS data cannot robustly discriminate between one- and two-component models with the current stellar models. In contrast, model fidelity is substantially better in the WFC3 near-infrared bands, where the evidence for multi-component photospheres is strongest.

5.2. Robust Evidence for Multi-Component Photospheres from WFC3

The WFC3/G102 and G141 retrievals consistently and significantly favor two-component models for HAT-P-11 reported in Table 3. This preference is not limited to a single epoch or instrumental configuration, but instead

Table 3. Retrieved Parameters from Two-component Fits to HAT-P-11 HST Spectra

Filter	T_1 (K)	T_2 (K)	f_2	R_{Star} (R_{\odot})	a_{scale}	$\ln f_{\text{var}}$
G430 [Not Preferred]	4625^{+17}_{-17}	4621^{+73}_{-116}	$0.170^{+0.218}_{-0.148}$	$0.793^{+0.006}_{-0.006}$	$0.962^{+0.017}_{-0.017}$	$-2.724^{+0.043}_{-0.042}$
G750 [Not Preferred]	4685^{+12}_{-8}	4662^{+63}_{-87}	$0.121^{+0.201}_{-0.101}$	$0.779^{+0.005}_{-0.005}$	$1.055^{+0.014}_{-0.015}$	$-4.300^{+0.023}_{-0.024}$
G102 [Preferred]	4966^{+33}_{-41}	3617^{+125}_{-149}	$0.264^{+0.038}_{-0.043}$	$0.782^{+0.007}_{-0.007}$	$0.991^{+0.013}_{-0.013}$	$-4.710^{+0.069}_{-0.069}$
G141 [Preferred]	4950^{+32}_{-27}	3326^{+110}_{-119}	$0.282^{+0.045}_{-0.051}$	$0.802^{+0.015}_{-0.016}$	$0.989^{+0.014}_{-0.013}$	$-4.722^{+0.073}_{-0.070}$
G102 + G141 [Preferred]	4979^{+20}_{-24}	3412^{+77}_{-73}	$0.259^{+0.020\dagger}_{-0.023}$	$0.800^{+0.011}_{-0.010}$	$0.954^{+0.024\dagger}_{-0.023}$	$-4.709^{+0.068\dagger}_{-0.074}$
	-	-	$0.331^{+0.041\dagger}_{-0.046}$	-	$1.005^{+0.019\dagger}_{-0.018}$	$-4.478^{+0.074\dagger}_{-0.065}$

NOTE—[†]For the combined G102+G141 fit, the first row lists the G102 parameters and the second row the G141 ones.

persists over a multi-year baseline, indicating that the result is not an artifact of instrument systematics or local time variability. Moreover, the overall agreement between model and data across the full WFC3 wavelength range (Figure 6) supports the robustness of these fits.

For both WFC3 gratings, the preferred two-component models yield a second-component temperature (T_2) that is approximately 1500 K lower than that of the first component (T_1), consistent with umbral-like temperatures (cf. the K0 dwarf simulations of Smitha et al. 2025). The temperature of the first component is slightly higher than the stellar effective temperature, as expected if the effective temperature were averaging over unresolved spot contributions.

Comparing the best-fitting one- and two-component models, the improvement of the two-component models is not driven by isolated spectral features but by subtle, broadband differences across the near-infrared bandpass. Although these differences are comparable in scale to the observational uncertainties, they are coherent across wavelength. Extending the analysis to optical wavelengths could, in principle, help discriminate between the one- and two-component models; however, as discussed in Section 5.1, current stellar spectra models are less reliable in that regime, limiting the robustness of such a comparison.

5.3. Comparison with Previous Studies

Several past studies have examined the surface inhomogeneities of HAT-P-11 using precise Kepler photometry Sanchis-Ojeda & Winn (2011); Béky et al. (2014); Morris et al. (2017a). In particular, the comprehensive analysis by Morris et al. (2017a) identified the active latitudes near $\sim 16^\circ$ and inferred that 0.5–10% of the transit chord covered by spots from transit to transit, with a median estimate of $3^{+6}_{-1}\%$ (Morris et al. 2017a). Although the inferred spot covering fractions from spot crossings exhibit a long tail toward higher values, these chord-based covering fractions are still sub-

stantially smaller than our disk-integrated estimates of $25.9^{+2.0}_{-2.3}\%$ for G102 and $33.1^{+4.0}_{-4.6}\%$ for G141 (see Table 4).

However, constraints on stellar surface inhomogeneities derived from spot-crossing events are subject to their own unique biases and degeneracies. First, spot crossings probe only the transit chords, which for HAT-P-11 spans a broad range of latitudes but, of course, does not sample the full stellar surface in a given transit. Moreover, despite the exquisite precision of Kepler short-cadence data (58.85 s), the photometry often lacks the resolution needed to capture substructure within starspots. As a result, modeling spots as single circular features on the stellar surface is subject to strong degeneracies between their size and position (Morris et al. 2017a). Second, if HAT-P-11 hosts a large population of small spots (similar to the “polka-dotted” configuration proposed for TRAPPIST-1 (Rathcke et al. 2025)), their signals may fall below the photometric detection threshold. Consequently, spot-covering fractions (f_2) inferred from spot-crossing events should be interpreted as lower limits, as they primarily trace large, high-contrast structures (e.g., Murray & Berta-Thompson 2025).

Using a different approach, Morris et al. (2019) analyzed TiO molecular bands in high-resolution optical spectra and inferred a filling factor of $15 \pm 6\%$. Their method decomposed the spectra into contributions from photospheric and spot components but fixed the spot temperature (assuming a TiO-forming temperature near 3300 K) and relied on a narrow wavelength range (7052–7062 Å), much smaller than the WFC3 bandpasses used here. In addition, their retrieval imposed a Gaia color prior that disfavors large filling factors. For stars with ~ 20 –30% spot coverage and several percent temporal variability, the nominal Gaia photometric uncertainty of 0.006 may underestimate the level of spot-induced modulation. Moreover, as discussed in Section 5.1, stellar spectral models in the optical remain imperfect, warranting caution when interpreting constraints derived in

that regime. We introduce a relatively weak constraint in our fit by incorporating B - and V -band fluxes in our fit, which have larger uncertainties than Gaia measurements. While stronger priors could similarly suppress large filling factors in our retrievals, doing so would risk introducing biases.

Estimates of the spot temperature contrast also vary in the literature. Simultaneous *Kepler–Spitzer* spot-crossing analyses by [Fraine et al. \(2014\)](#) yielded a spot-photosphere temperature contrast of 900 ± 300 K⁹. By contrast, multi-band optical photometry by [Schutte et al. \(2023\)](#) suggested a substantially smaller contrast of ~ 250 K. The latter study relies on ground-based optical photometry, where the precision and systematics are often comparable to the amplitudes of spot-crossing signals themselves, potentially limiting the robustness of the inferred contrasts. Additionally, the apparent temperature contrast depends on which portion of the spot is occulted during transit, with umbral crossings producing larger apparent contrasts than penumbral crossings.

5.4. Evidence for Long-Term Variability in Stellar Activity

Our spectral retrievals indicate different spot filling factors between the 2012 G141 and 2016 G102 observations ([Figure 4](#)), suggesting a possible secular decline in stellar activity over this period. Motivated by this trend, we examine independent activity diagnostics to assess whether they support a similar long-term evolution.

5.4.1. Long-Term Evolution of the Ca II H&K index

The strongest independent evidence for a magnetic activity cycle in HAT-P-11 comes from long-term monitoring of the Ca II H&K S-index using Keck/HIRES and APO/ARCES spectroscopy ([Morris et al. 2017b](#)). These measurements show variability in both rotational and multiyear timescales. The data are consistent with a long-duration (≥ 10 years) activity cycle in which HAT-P-11 remained near an activity maximum during the Kepler era, declined toward a minimum around 2016, and began rising again by 2017. This temporal evolution broadly mirrors our spectroscopic results: higher spot filling factors during the G141 epoch (near the Kepler era) and lower values during the G102 observations in 2016 (see [Figure 7](#)).

Given that HAT-P-11 is a main-sequence K dwarf broadly similar to the Sun but substantially more active, we can also use empirical relations between chromospheric activity and spot coverage derived from solar ob-

servations to place our results in context. Applying the solar-calibrated relation of [Sowmya et al. \(2023, Eq. 7\)](#) to the observed S -index measurements implies a spot coverage of ~ 30 – 40% during the activity maximum, in close agreement with our results. However, extrapolating such relations from the Sun to a cooler, more active K dwarf is non-trivial. Moreover, Ca II H&K emission predominantly traces chromospheric plage rather than photospheric spots (e.g., [Cretignier et al. 2024](#)); while plages and spots are correlated, the spot-to-faculae ratio is known to vary with activity level ([Shapiro et al. 2014](#)), potentially biasing spot coverage estimates inferred from Ca II H&K.

Recent S -index monitoring of HAT-P-11 extends the Ca II H&K baseline and shows that the star approached one of its lowest measured activity levels around 2024 ([Morris et al. 2025](#)). This low-activity phase coincides with the JWST observations, suggesting those spectra were acquired near a relative minimum in stellar activity.

5.4.2. Evidence from Photometric Time Series

The four-year Kepler light curve exhibits rotational modulation amplitudes ranging from $\sim 1.44\%$ to $\sim 2.15\%$, indicating temporal evolution of the stellar surface. TESS extends the temporal baseline with eleven sectors of observation, albeit in a redder bandpass, with rotational amplitude ranging from $\sim 0.15\%$ to $\sim 0.97\%$.

Using the spot temperatures retrieved from our multi-component spectral fits, we estimate the wavelength-dependent spot contrast in the Kepler and TESS bandpasses. We obtain $C_{\text{Kepler}} = 0.933 \pm 0.011$ and $C_{\text{TESS}} = 0.869 \pm 0.016$, corresponding to a contrast ratio of 1.0735 ± 0.0073 between the bands. For a K4 dwarf, this implies that only modest differences in rotational modulation amplitude are expected between the bluer Kepler and redder TESS bandpasses ($\sim 10\%$ changes). The observed decline in modulation amplitude from Kepler to TESS ([Figure 1](#)), therefore, cannot be explained by bandpass effects alone.

To translate photometric amplitudes into spot covering fractions, we adopt the scaling relation of [Rackham et al. \(2019, Eq. 2\)](#), in which the rotational modulation amplitude scales approximately as the square root of the spot filling factor. We measure Kepler rotational modulation amplitudes at the difference between the 5th and 95th percentile flux values within continuous observing windows separated by no more than 10 days. Using the contrast coefficient appropriate for K4 dwarfs ($C = 0.048 \pm 0.020$, defined as $F_{\text{spot}}/F_{\text{phot}}$ in that work), the peak-to-peak Kepler amplitude of $\sim 2\%$ implies a characteristic spot filling factor of order $\sim 20\%$, albeit with a broad allowed range, given the uncertainty

⁹ Error estimated from their [Figure 1](#).

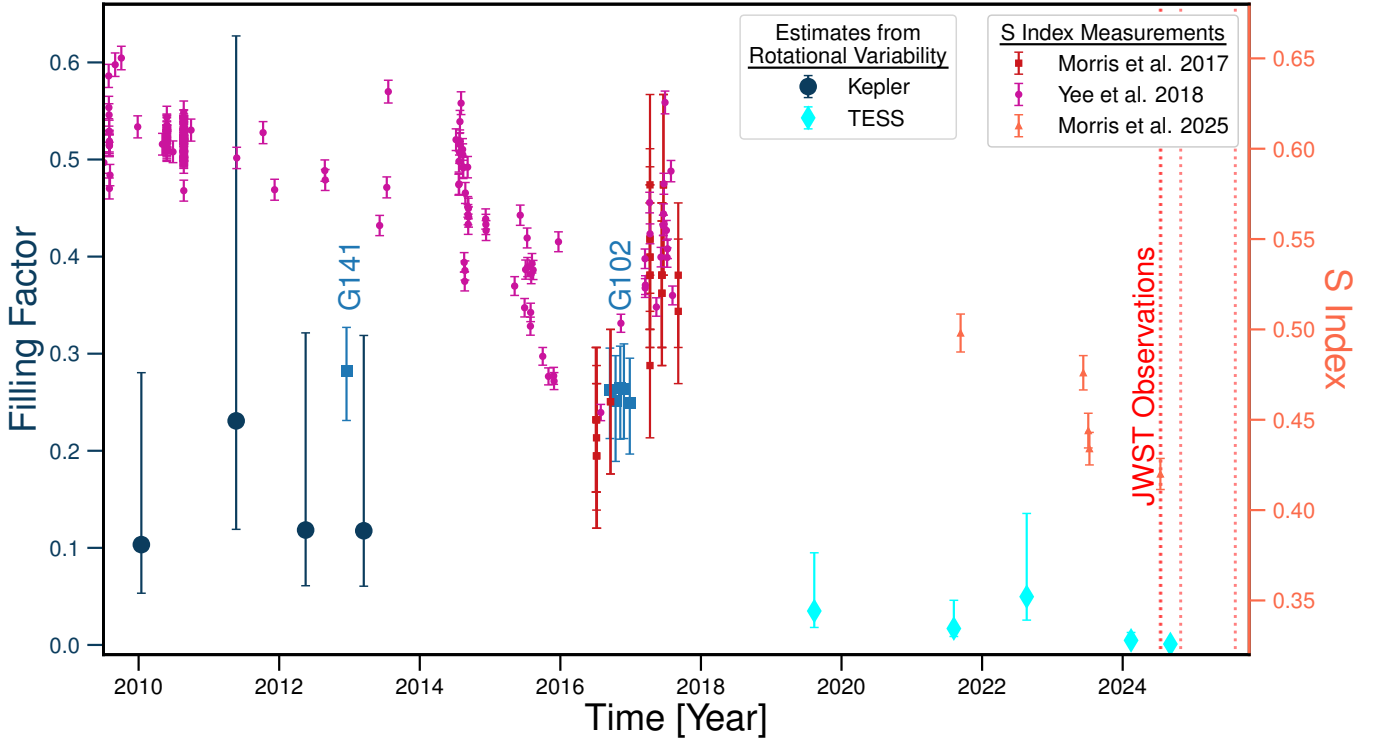


Figure 7. Spot filling factors of HAT-P-11 as a function of time. Filling factors derived from rotational variability in Kepler and TESS light curves (using Equation 2 of Rackham et al. 2019) are compared with values inferred from multi-component spectral fits to HST G102 and G141 data. Independent chromospheric activity measurements (S-index values from the literature) are shown on the right axis. The Kepler era exhibits relatively high filling factors with substantial variability, whereas the TESS epochs indicate a transition to markedly lower spot coverage. Red vertical dotted lines mark the epochs of JWST observations.

in C driven by the intrinsic degeneracies of spot distributions. Nonetheless, this estimate is broadly consistent with our WFC3 inferences.

Applying the same procedure to TESS data reveals amplitudes of $\sim 1\%$ in early sectors, decreasing to $\sim 0.2\%$ in later sectors. Corresponding inferred spot filling factors are of the order of a few percent. This photometric evolution is generally consistent with the behavior of the Ca II H&K index and supports the interpretation that the star entered a lower-activity state by 2024, before the JWST observations.

5.5. Forward Modeling of Rotational Modulation

To further interpret the relationship between rotational modulation amplitude and spot coverage, we performed a suite of forward simulations using `spotter` (Garcia et al. 2025). We generated ensembles of synthetic stellar surfaces with randomly located spots and computed the resulting light curves. In this framework, each spot is modeled as a circular feature with a smooth, sigmoid-like edge rather than a hard boundary. We considered two characteristic spot sizes: small spots (angular radii $\leq 0.6^\circ$) and medium spots ($0.6\text{--}3^\circ$), with sharpness drawn from a uniform distribution of

$\mathcal{U}(10, 50)$. Our simulated spot contrasts are representative of those expected in Kepler bandpass (~ 0.93) based on our retrieved temperature. The resulting dispersion of the rotational amplitude is driven by the variability in spot configurations, which are an order of magnitude larger than the bandpass-dependent effects between Kepler and TESS. Thus, the same amplitude–filling factor relation remains applicable to TESS data to a good approximation.

The simulated rotational amplitude shows a roughly square-root scaling with respect to filling factor for both small spots (angular radii $\leq 0.6^\circ$) and medium spots ($0.6\text{--}3^\circ$), as shown in Figure 8. The observed Kepler ($\sim 2\%$) and early TESS ($\sim 1\%$) rotational amplitudes are thus consistent with the spot covering fractions inferred from the HST/WFC3 retrievals ($f_{G102} \sim 0.26$, $f_{G141} \sim 0.33$), which predict rotational modulations at the few-percent level during active phases. For rotational amplitudes $\gtrsim 1\%$, the filling factor is only weakly constrained due to strong degeneracies with spot size and latitudinal distribution. In contrast, the very low amplitudes observed in later TESS sectors tightly rule out large filling factors, indicating a markedly less spotted photosphere.

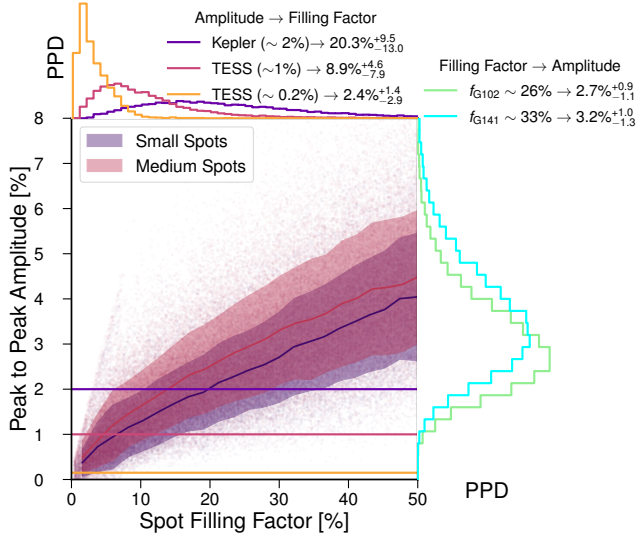


Figure 8. Peak-to-peak rotational modulation amplitude as a function of spot filling factor from ensembles of simulated stellar surface realizations. Colored curves and shaded regions show the median relation and dispersion for small-spot (purple) and medium-spot (red) populations using `spotter`. Horizontal lines mark rotational amplitudes from Kepler ($\sim 2\%$) and TESS ($\sim 1\%$ and $\sim 0.2\%$), and the distribution of the corresponding filling factor to produce such amplitudes is shown on the top. Similarly, the retrieved filling factors from HST/WFC3 ($f_{G102} \sim 26\%$ and $f_{G141} \sim 33\%$) imply expected rotational amplitudes of $\sim 2\text{--}4\%$ in the Kepler band.

We also explored a light-curve inversion framework tailored to HAT-P-11. The system’s well-constrained stellar obliquity, orbital geometry, and active latitudes ($16 \pm 5^\circ$; Morris et al. 2017a) allow us to generate maximum-likelihood surface realizations using a surface Gaussian process and Matérn-3/2 kernel. For each surface map, we computed the corresponding light curve and optimized the fit to the data using Nelder–Mead minimization. Owing to strong degeneracies inherent to the light curve inversion problem, the inferred maps in the middle panel for Figure 9 are illustrative rather than unique solutions. They demonstrate plausible spot distributions consistent with the light curves.

At the same time, visual inspection of the corresponding transit light curves (right column of Figure 9) reveals prominent spot-crossing anomalies in the Kepler data but none in TESS. Although TESS photometry is less precise, spot crossings comparable in amplitude to those observed in Kepler data should still be detectable. Their absence therefore supports a reduced level of spot-induced structure on HAT-P-11 during the TESS epoch relative to the Kepler era.

5.6. Comparison to Other K dwarfs

To place the inferred spot properties of HAT-P-11 in context, we compare them with those of other active K-dwarf exoplanet hosts. A useful reference is HD 189733 (K2V compared to K4V for HAT-P-11), which exhibits exceptionally high spot coverage from $38 \pm 4\%$ to $47 \pm 3\%$, similarly inferred from HST/WFC3/G141 spectra (N24). More broadly, mid-to-late K dwarfs in the Kepler sample exhibit large photometric modulation amplitudes $\sim 0.3\text{--}1.7\%$ (McQuillan et al. 2014; Rackham et al. 2019), generally consistent with spot filling factors of tens of percent (Rackham et al. 2019). In this context, the 20–30% filling factors inferred for HAT-P-11 fall within the upper range expected for active K dwarfs, but are not wholly unprecedented. Similarly, empirical relations predict $T_{\text{spot}} \sim 3588$ K for HAT-P-11 (Berdyugina 2005), with updated fits giving 3680 ± 420 K ($\Delta T = 1100 \pm 420$ K; Herbst et al. 2021), consistent with our inferred T_2 .

Turning to more precise and reliable JWST observations, recent studies further indicate that substantial spot coverage is common among K-dwarf hosts. For example, the K2V hosts HAT-P-18 and WASP-52—both spectrally comparable to the K4V HAT-P-11—show prominent spot crossings in their transit observations (Fournier-Tondreau et al. 2024, 2025). In the case of WASP-52, two distinct two-spot crossing events with different inferred temperatures were detected during a single JWST transit, corresponding to a filling factor of $30 \pm 10\%$. Similarly, the slightly late-type K7V star GJ 9827 shows evidence for spot coverage at the $\sim 10\%$ level (Piaulet-Ghorayeb et al. 2024).

Taken together, these results indicate that HAT-P-11 may not be exceptional among active K dwarfs in having a large spot filling factor. Rather, substantial photospheric heterogeneity appears to be a normal property of magnetically active K-dwarf planet hosts.

5.7. Impact on the Stellar Radius

As described in Section 3.3, we fit for the stellar radius and distance, adopting Gaussian priors from Bakos et al. (2010) and Gaia Collaboration et al. (2023), respectively. Broadband photometric fluxes constrain the absolute flux normalization of the HST spectra, which depends jointly on the stellar radius, distance, and an overall scaling factor. Because the Gaia distance is precisely known compared to stellar radius, the remaining freedom is largely captured by a degeneracy between the stellar radius and the flux scaling factor such that smaller radii can offset larger scale factors (and vice versa; see Figure 10).

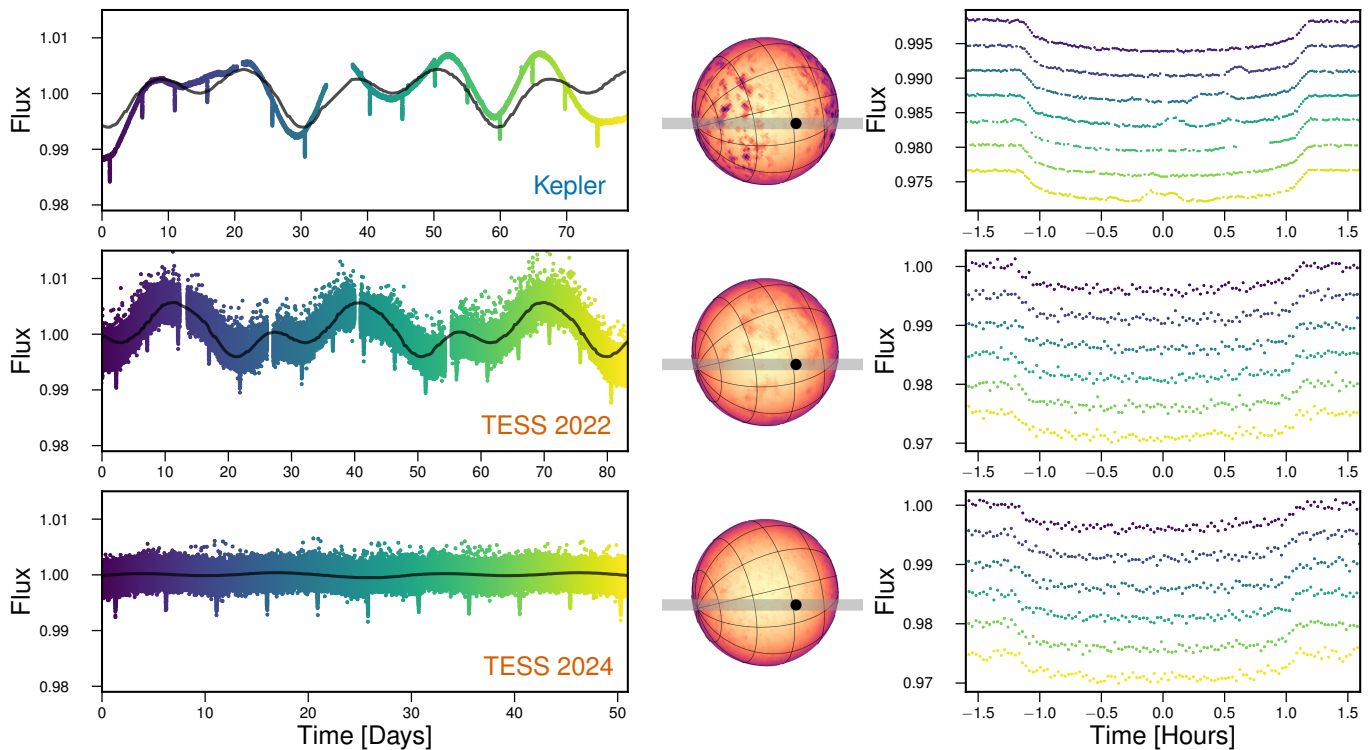


Figure 9. Evolution of stellar activity for HAT-P-11 across observing epochs. **Left:** Photometry during the Kepler active phase and two TESS epochs. The Kepler data show strong rotational modulation, while the 2022 and 2024 TESS data show reduced variability and minimal modulation, respectively. Black curves represent example forward-model realizations using *spotter* (Garcia et al. 2025) that roughly model the spot configuration without accounting for temporal evolution. **Middle:** Representative stellar surface maps corresponding to the *spotter* light curves, illustrating decreasing spot coverage across epochs. **Right:** Vertically offset transit light curves from the same epochs (every other transit shown). Spot-crossing anomalies are prominent in the Kepler data but not observed in the TESS data, owing to reduced contrast and higher noise levels. The TESS light curves are binned for clarity.

In the literature, stellar radii are commonly estimated by fitting single-component models to broadband SED photometry, typically achieving uncertainties at the ~ 5 - 10% level (Stassun et al. 2019). However, interferometric measurements of K- and M-dwarfs have often yielded radii systematically larger than those inferred from SED fits and theoretical predictions, with discrepancies on the order of a few percent and reaching $\sim 2\sigma$ in some cases (e.g., Boyajian et al. 2012).

While various explanations have been suggested for this, one plausible contributor to this discrepancy is neglecting surface heterogeneity, particularly for active stars. Multi-component photospheres redistribute flux across wavelength in a way that could systematically bias the radius inferred under the assumption of a single-component model. For HAT-P-11, our inferred stellar radius is consistent with the prior adopted from the literature (Bakos et al. 2010). The resulting uncertainty is modestly reduced, reflecting the additional constraints provided by our data within our prior-informed framework. Conceptually, our results suggest that larger spot

filling factors typically tend to increase the inferred stellar radius (provided the photospheric temperature is well constrained), as cooler components would have to be compensated by a larger emitting area for the observed flux. To robustly establish the impact of multi-component models will require a broader population-level analysis and independent validation (e.g., via interferometric measurements), which is beyond the scope of this work, although our results provide a strong motivation for their consideration in inferring stellar radii.

6. IMPLICATIONS FOR TRANSMISSION SPECTROSCOPY

Observations of HAT-P-11 have long shown a discrepancy between the transit depths measured with HST and *Spitzer*. In particular, Fraine et al. (2014) reported a prominent $1.4\ \mu\text{m}$ H_2O feature and argued that the spot-photosphere contrast would render starspots too warm to produce significant water absorption. However, when combining broader wavelength coverage with *Spitzer* data, Chachan et al. (2019) found that reconciling the shallower *Spitzer* depths requires a $\sim 3\%$

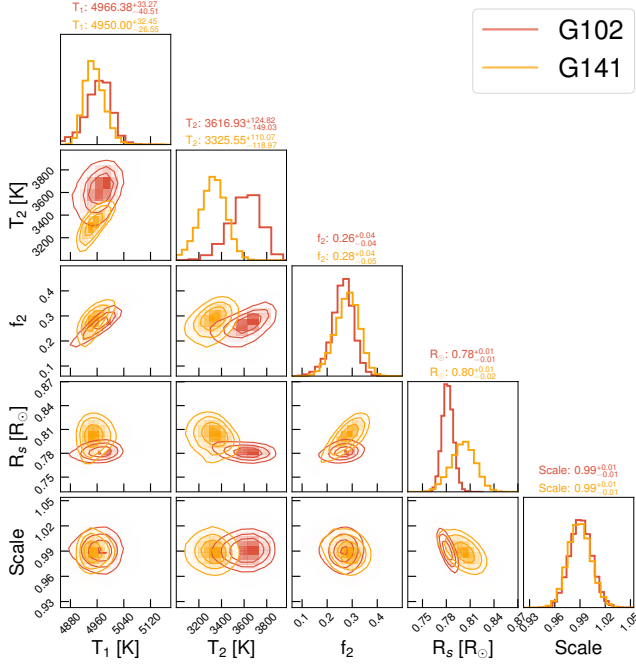


Figure 10. Corner plot illustrating parameter degeneracies in the two-component spectral fits to the WFC3/G102 (red) and G141 (orange) data. Shown are posterior distributions for the photospheric temperature (T_1), spot temperature (T_2), spot filling factor f_2 , stellar radius (R_s), and the flux scale factor.

brightening of the stellar disk under the assumption of $T_{\text{spot}} = 4500$ K, which they considered implausible given prior estimates of the stellar inhomogeneities of HAT-P-11. In contrast, Cubillos et al. (2022) allowed inter-instrument offsets to vary within the retrieval framework and found that such offsets substantially impact the retrieved parameters for HAT-P-11.

Given our inference of substantial spot coverage, we model the effect of stellar contamination in this system. Following Rackham et al. (2018), we express the observed transit depth as

$$D_{\lambda,\text{obs}} = \epsilon_{\lambda} D_{\text{True}} \quad (6)$$

where D_{True} is the intrinsic planetary transit depth and ϵ_{λ} is a wavelength-dependent contamination factor determined by the contrast between the transit-chord and disk-integrated stellar spectra. Allowing spots to be present in the transit chord but at a different level than

on the stellar disk, ϵ_{λ} is given by

$$\epsilon_{\lambda} = \frac{(1 - f_{\text{spot}})S_{\lambda,\text{phot}} + f_{\text{spot}}S_{\lambda,\text{spot}}}{(1 - F_{\text{spot}})S_{\lambda,\text{phot}} + F_{\text{spot}}S_{\lambda,\text{spot}}} \quad (7)$$

$$= \frac{1 - f_{\text{spot}} \left(1 - \frac{S_{\lambda,\text{spot}}}{S_{\lambda,\text{phot}}}\right)}{1 - F_{\text{spot}} \left(1 - \frac{S_{\lambda,\text{spot}}}{S_{\lambda,\text{phot}}}\right)}, \quad (8)$$

where f_{spot} and F_{spot} are the transit-chord and disk-integrated spot filling factors, respectively, and $S_{\lambda,\text{spot}}$ and $S_{\lambda,\text{phot}}$ are the spectra of the spot and photosphere, respectively (Zhang et al. 2018).

Using spot temperatures and filling factors derived from our spectral retrievals and assuming the transit-chord and full-disk filling factors are independent realizations of the spot filling factor constraint, we compute the expected contamination signal across 0.3–5.0 μm (Figure 11). The resulting contamination amplitudes are comparable to the observed spectral features, including the ~ 100 ppm offset between HST and *Spitzer*. This implies that stellar heterogeneity alone could account for features previously attributed to planetary atmospheric structure. While the detection of water vapor in the WFC3/G141 data remains robust—being driven primarily by a single high-quality epoch—the joint interpretation of multi-epoch, multi-instrument datasets without contemporaneous stellar constraints is vulnerable to bias. When stellar contamination can be comparable in amplitude to planetary spectral features, retrieval outcomes depend sensitively on how stellar surface structure is treated.

6.1. Re-evaluation of HST+Spitzer Results

Before JWST, transmission spectroscopy commonly relied on combining observations from multiple instruments or telescopes to extend spectral coverage (e.g., Chachan et al. 2019). This strategy was driven by instrumental bandpass limitations rather than scientific preference. However, stitching together data obtained at different epochs implicitly assumes a stable stellar photosphere, unless explicitly modeled otherwise.

In the analysis of Chachan et al. (2019), stellar contamination corrections were applied using strong priors on spot filling factor and fixed spot temperatures (4100–4500 K). The adopted filling factor of 4.4% during the G102 epoch was motivated by spot-crossing constraints from (Morris et al. 2017a), which, according to our analysis, likely underestimate the total disk-integrated heterogeneity. By contrast, a later independent analysis (Cubillos et al. 2022) treated inter-instrument offsets as free parameters, effectively allowing for changes in stellar brightness due to heterogeneity. These differing

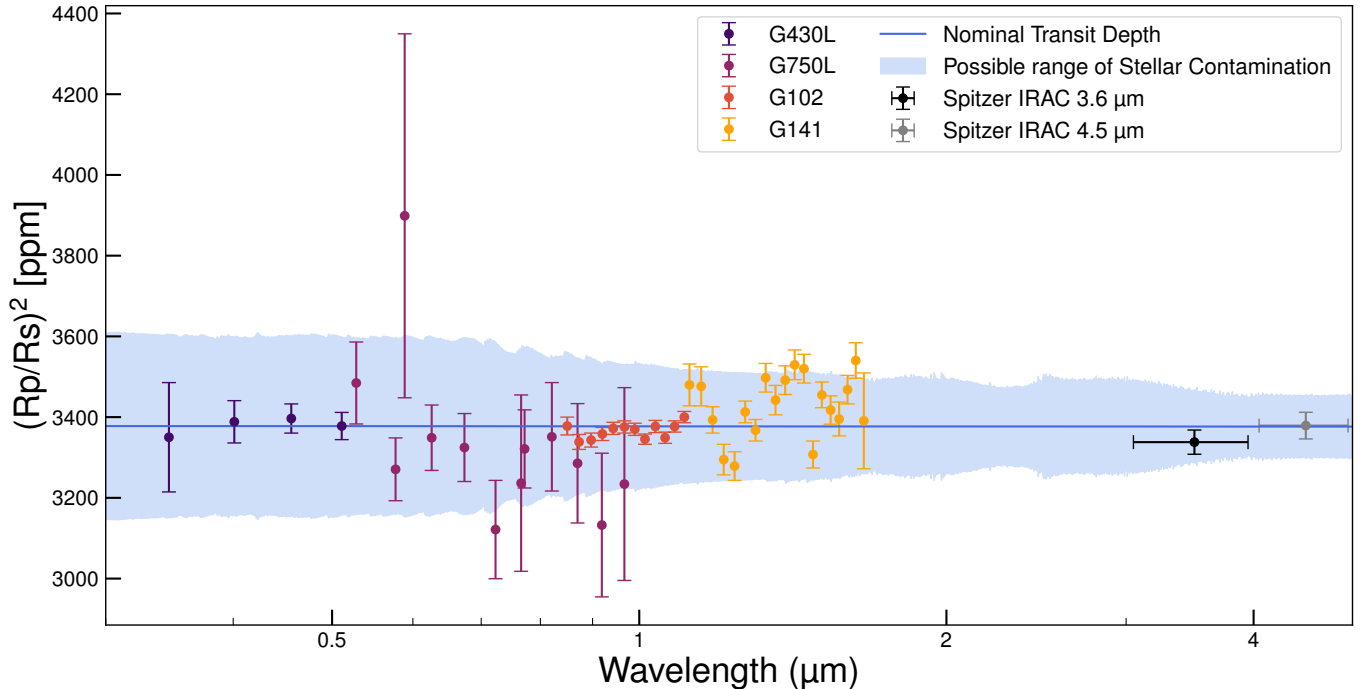


Figure 11. Range of possible stellar contamination signals due to HAT-P-11’s photospheric heterogeneity. The multi-instrument 0.3–5.0 μm transmission spectrum of HAT-P-11 (Chachan et al. 2019) is shown alongside the 68% confidence interval for the expected contribution from stellar contamination (light blue region), assuming a nominal planetary transit depth (blue line). The amplitude of possible stellar contamination signals is comparable to the observed spectral features, including the ~ 100 ppm offset between the HST and *Spitzer* observations. This implies that atmospheric retrievals that neglect stellar contamination are susceptible to significant biases.

treatments of unmodeled stellar contamination lead to inconsistent atmospheric inferences.

Our results show that contamination signals of order 100 ppm arise naturally from plausible spot configurations (Figure 11). In this regime, unmodeled stellar heterogeneity can directly bias retrieved molecular abundances and atmospheric structure. The challenge is not the detection of spectral features themselves, but the reliable attribution of those features to planetary rather than stellar origins.

6.2. Lessons for Future Observations

The JWST era has transformed transmission spectroscopy: molecular bands that once required stitching together data from multiple facilities to study can now be detected at exquisite precision within a single visit. Programs such as ongoing JWST GO programs 4105 (PI: Lilli Anderson), 2950 (PI: Ren Waters), and 5924 (PI: David Sing) illustrate this growing capability. However, this sharp increase in precision has also exposed significant limitations in earlier assumptions regarding stellar contamination. Our results demonstrate that stellar heterogeneity can imprint spurious spectral structure even beyond the 1–2 μm regime, challenging the common assumption that near- and mid-infrared

transmission spectra are largely immune to stellar effects.

It is perhaps inevitable that the most compelling atmospheric signals are also the most challenging to interpret. As the field pushes toward detecting subtle features, such as weak molecular bands or hemispheric asymmetries (Espinoza et al. 2024), the influence of stellar surface structure becomes increasingly non-negligible (Kostogryz et al. 2024, 2025). While the broad spectroscopic coverage of JWST enables retrievals anchored by multiple molecular bands and continuum regions, our results show that stellar inhomogeneities can fundamentally limit the robustness of such inferences. Retrievals can recover atmospheric parameters only when stellar contamination is explicitly modeled; neglecting stellar heterogeneity leads to biased molecular abundances (Iyer & Line 2020). High-resolution cross-correlation techniques are somewhat more resilient to stellar contamination, but even these methods can be more challenging once realistic spot contrasts and spatial distributions are included (Bourrier et al. 2024).

Building on our ongoing efforts with HST to characterize stellar surfaces for a set of high-priority exoplanet hosts, we will extend this work using out-of-transit JWST observations as part of GO-AR-5370 (PI: Rack-

ham)¹⁰. Jointly fitting for out-of-transit stellar spectra alongside transmission spectra will enable epoch-specific constraints on stellar heterogeneity, providing a pathway toward mitigating stellar contamination and achieving more robust atmospheric retrievals. Complementary photometric monitoring or activity diagnostics (such as Ca II H&K) could further identify optimal windows for transmission spectra even for active hosts.

7. CONCLUSIONS

We have presented a comprehensive analysis of the disk-integrated photospheric heterogeneity of HAT-P-11 using multi-epoch, absolutely calibrated out-of-transit spectra from HST/STIS and HST/WFC3, spanning 0.3–1.7 μm . By combining these data with broadband photometry, long-term Kepler and TESS monitoring, chromospheric activity indices, and forward modeling of stellar variability, we quantify the time-dependent photospheric heterogeneity of HAT-P-11 and its impact on transmission spectroscopy.

Our main conclusions are as follows.

1. The near-infrared spectra point to a heterogeneous photosphere. For all HST/WFC3 epochs, two-component photospheric models are strongly preferred over single-component fits, with $\Delta\text{BIC} \sim 10$ indicating robust evidence for a cooler surface component. The preferred solutions consist of a dominant component of $T_1 \approx 4980\text{ K}$ and a cooler component of $T_2 \approx 3400\text{ K}$, with filling factors of $f_2 \approx 0.26\text{--}0.33$. The consistency across independent WFC3 modes and epochs indicates that substantial photospheric heterogeneity is required to model the disk-integrated near-infrared spectrum.
2. Inferences from optical spectra are limited by model fidelity challenges. The STIS G430L/G750L spectra do not statistically favor multi-component models. However, comparisons between available atmospheric models reveal $>2\%$ discrepancies in the optical, indicating that model uncertainties dominate at these wavelengths. The lack of a multi-component preference in the optical therefore likely reflects model fidelity limitations rather than evidence for a homogeneous photosphere, highlighting the need for targeted model improvements in the optical regime.
3. HAT-P-11 was highly spotted during the HST epochs. The inferred filling factors of 26–33% exceed estimates derived from transit chord anal-

yses, implying that a significant fraction of the spotted area lies outside the transit chord or consists of smaller-scale structures not resolved in spot-crossing events. These values, however, are more consistent with previous disk-integrated TiO-based analyses. The inferred temperature contrast ($\Delta T \approx 1500\text{ K}$) is consistent with cool, umbra-like regions on active K dwarfs.

4. Independent diagnostics confirm substantial temporal evolution in the spottedness of HAT-P-11. The HST observations (2012–2016) occurred during a relatively active phase, coinciding with Kepler rotational modulation amplitudes of $\sim 2\%$ and elevated Ca II H&K emission. In contrast, later TESS observations show reduced variability of $\sim 1\%$ and as low as $\sim 0.2\%$ in the final sector, accompanied by a decline in the S-index. By 2024, the implied spot coverage had decreased to only a few percent. The JWST observations coincided with this lower-activity phase, and are thus expected to be less impacted by stellar contamination, though non-negligible biases remain possible with spot coverage at the $\sim 2\text{--}10\%$ level.
5. The amplitude of plausible stellar contamination signals is comparable to planetary spectral features. Using the retrieved spot temperatures and filling factors, we compute contamination signals of order $\sim 100\text{ ppm}$ across 0.3–5 μm . This is comparable to the amplitude of key transmission spectral features and to the previously reported HST–*Spitzer* offset. Atmospheric retrievals that neglect stellar heterogeneity are therefore susceptible to significant biases, particularly when combining multi-epoch or multi-instrument datasets.

HAT-P-11 provides a valuable testbed for modeling stellar surface heterogeneity using precise, space-based out-of-transit spectroscopy. Constraining the stellar surface properties during transit and propagating these constraints into transmission spectroscopy analyses enables more robust interpretations of planetary atmospheres. The methodology developed here, combining absolute spectrophotometry, activity diagnostics, and forward contamination modeling, provides a framework that can be applied to other transiting planet hosts.

We are extending this approach through the HST Stellar Treasure Trove and the Eyes on the Stars Legacy Archival Programs, which are analyzing a broader sample of planet-hosting stars observed with both HST and JWST to enable population-level insights on stellar surface inhomogeneities. Complementary long-term, high-resolution spectroscopic monitoring (e.g., the OWLS

¹⁰ <https://jwst-eots.github.io/>

program; Morris et al. 2025) and rotational modulation measurements from TESS can further contextualize the state of the stellar photosphere at the time of transit observations. The recently launched *Pandora Small-Sat Mission* (Quintana et al. 2024), designed specifically to constrain the properties of both active K- and M-dwarf host stars and their transiting exoplanets, will further provide critical context for interpreting transmission spectra (Rackham et al. 2026; Rotman et al. 2026).

While stellar contamination remains one of the central challenges for transmission spectroscopy, stellar surface characterization via space-based spectroscopy now offers a clear path towards robust atmospheric inferences in the JWST era. The results presented here show further that for some active stars, there may be times when lower activity states provide better windows for transmission spectroscopy.

Facilities: *HST*, *Kepler*, *TESS*,

Software: `speclib` (Rackham 2023), `PACMAN` (Zieba & Kreidberg 2022), `spotter` (Garcia et al. 2025)

ACKNOWLEDGMENTS

The authors thank Prof. Sara Seager, Dr. Ana Glidden, Dr. Rachael C. Amaro, and Dr. Veronika Witzke for helpful discussions and constructive input on this work. Based on observations with the NASA/ESA Hubble Space Telescope obtained from the Mikulski Archive for Space Telescopes (MAST) at the Space Telescope Science Institute, which is operated by the Association of Universities for Research in Astronomy, Incorporated, under NASA contract NAS5-26555. Support for program number HST-AR-17551 was provided through a grant from the STScI under NASA contract NAS5-26555. This paper includes data collected by the Kepler and TESS missions, obtained from the Mikulski Archive for Space Telescopes (MAST). Funding for the Kepler and TESS missions is provided by the NASA Science Mission Directorate. This material is based upon work supported by the National Aeronautics and Space Administration under Agreement No. 80NSSC21K0593 for the program “Alien Earths”. The results reported herein benefited from collaborations and/or information exchange within NASA’s Nexus for Exoplanet System Science (NExSS) research coordination network sponsored by NASA’s Science Mission Directorate. This material is based upon work supported by the European Research Council (ERC) Synergy Grant under the European Union’s Horizon 2020 research and innovation program (grant No. 101118581—project REVEAL).

REFERENCES

- Anderson, T. W., & Darling, D. A. 1954, *Journal of the American Statistical Association*, 49, 765, doi: [10.1080/01621459.1954.10501232](https://doi.org/10.1080/01621459.1954.10501232)
- Andretta, V., Busà, I., Gomez, M. T., & Terranegra, L. 2005, *A&A*, 430, 669, doi: [10.1051/0004-6361:20041745](https://doi.org/10.1051/0004-6361:20041745)
- Bakos, G. Á., Torres, G., Pál, A., et al. 2010, *ApJ*, 710, 1724, doi: [10.1088/0004-637X/710/2/1724](https://doi.org/10.1088/0004-637X/710/2/1724)
- Barkaoui, K., Timmermans, M., Soubkiou, A., et al. 2023, *A&A*, 677, A38, doi: [10.1051/0004-6361/202346838](https://doi.org/10.1051/0004-6361/202346838)
- Basilicata, M., Giacobbe, P., Bonomo, A. S., et al. 2024, *A&A*, 686, A127, doi: [10.1051/0004-6361/202347659](https://doi.org/10.1051/0004-6361/202347659)
- Béky, B., Kipping, D. M., & Holman, M. J. 2014, *MNRAS*, 442, 3686, doi: [10.1093/mnras/stu1061](https://doi.org/10.1093/mnras/stu1061)
- Berdugina, S. V. 2005, *Living Reviews in Solar Physics*, 2, 8, doi: [10.12942/lrsp-2005-8](https://doi.org/10.12942/lrsp-2005-8)
- Borucki, W. J., Koch, D., Basri, G., et al. 2010, *Science*, 327, 977, doi: [10.1126/science.1185402](https://doi.org/10.1126/science.1185402)
- Bourrier, V., Delisle, J.-B., Lovis, C., et al. 2024, *A&A*, 691, A113, doi: [10.1051/0004-6361/202449203](https://doi.org/10.1051/0004-6361/202449203)
- Boyajian, T. S., von Braun, K., van Belle, G., et al. 2012, *ApJ*, 757, 112, doi: [10.1088/0004-637X/757/2/112](https://doi.org/10.1088/0004-637X/757/2/112)
- Chachan, Y., Knutson, H. A., Gao, P., et al. 2019, *AJ*, 158, 244, doi: [10.3847/1538-3881/ab4e9a](https://doi.org/10.3847/1538-3881/ab4e9a)
- Cretignier, M., Pietrow, A. G. M., & Aigrain, S. 2024, *MNRAS*, 527, 2940, doi: [10.1093/mnras/stad3292](https://doi.org/10.1093/mnras/stad3292)
- Cubillos, P. E., Harrington, J., Blečić, J., et al. 2022, *PSJ*, 3, 81, doi: [10.3847/PSJ/ac348b](https://doi.org/10.3847/PSJ/ac348b)
- Cushing, M. C., Vacca, W. D., & Rayner, J. T. 2004, *PASP*, 116, 362, doi: [10.1086/382907](https://doi.org/10.1086/382907)
- de Wit, J., Wakeford, H. R., Lewis, N. K., et al. 2018, *Nature Astronomy*, 2, 214, doi: [10.1038/s41550-017-0374-z](https://doi.org/10.1038/s41550-017-0374-z)
- Delrez, L., Murray, C. A., Pozuelos, F. J., et al. 2022, *A&A*, 667, A59, doi: [10.1051/0004-6361/202244041](https://doi.org/10.1051/0004-6361/202244041)
- Espinoza, N., Rackham, B. V., Jordán, A., et al. 2019, *MNRAS*, 482, 2065, doi: [10.1093/mnras/sty2691](https://doi.org/10.1093/mnras/sty2691)
- Espinoza, N., Steinrueck, M. E., Kirk, J., et al. 2024, *Nature*, 632, 1017, doi: [10.1038/s41586-024-07768-4](https://doi.org/10.1038/s41586-024-07768-4)

- Fournier-Tondreau, M., MacDonald, R. J., Radica, M., et al. 2024, *MNRAS*, 528, 3354, doi: [10.1093/mnras/stad3813](https://doi.org/10.1093/mnras/stad3813)
- Fournier-Tondreau, M., Pan, Y., Morel, K., et al. 2025, *MNRAS*, 539, 422, doi: [10.1093/mnras/staf489](https://doi.org/10.1093/mnras/staf489)
- Fraine, J., Deming, D., Benneke, B., et al. 2014, *Nature*, 513, 526, doi: [10.1038/nature13785](https://doi.org/10.1038/nature13785)
- Gaia Collaboration, Vallenari, A., Brown, A. G. A., et al. 2023, *A&A*, 674, A1, doi: [10.1051/0004-6361/202243940](https://doi.org/10.1051/0004-6361/202243940)
- Garcia, L., Rackham, B., & Panwar, V. 2025, *The Journal of Open Source Software*, 10, 8305, doi: [10.21105/joss.08305](https://doi.org/10.21105/joss.08305)
- Garcia, L. J., Moran, S. E., Rackham, B. V., et al. 2022, *A&A*, 665, A19, doi: [10.1051/0004-6361/202142603](https://doi.org/10.1051/0004-6361/202142603)
- Ghachoui, M., Soubkiou, A., Wells, R. D., et al. 2023, *A&A*, 677, A31, doi: [10.1051/0004-6361/202347040](https://doi.org/10.1051/0004-6361/202347040)
- Goudfrooij, P., & Christensen, J. A. 1998, *STIS Near-IR Fringing. III. A Tutorial on the Use of the IRAF Tasks*, *STIS Instrument Science Report 98-29*, 14 pages
- Hauschildt, P. H., Barman, T., Baron, E., Aufdenberg, J. P., & Schweitzer, A. 2025, *A&A*, 698, A47, doi: [10.1051/0004-6361/202554171](https://doi.org/10.1051/0004-6361/202554171)
- Herbst, K., Papaioannou, A., Airapetian, V. S., & Atri, D. 2021, *ApJ*, 907, 89, doi: [10.3847/1538-4357/abcc04](https://doi.org/10.3847/1538-4357/abcc04)
- Iyer, A. R., & Line, M. R. 2020, *ApJ*, 889, 78, doi: [10.3847/1538-4357/ab612e](https://doi.org/10.3847/1538-4357/ab612e)
- Iyer, A. R., Line, M. R., Muirhead, P. S., Fortney, J. J., & Faherty, J. K. 2025, arXiv e-prints, arXiv:2512.02269, doi: [10.48550/arXiv.2512.02269](https://doi.org/10.48550/arXiv.2512.02269)
- Iyer, A. R., Line, M. R., Muirhead, P. S., Fortney, J. J., & Gharib-Nezhad, E. 2023, *ApJ*, 944, 41, doi: [10.3847/1538-4357/acabc2](https://doi.org/10.3847/1538-4357/acabc2)
- Kostogryz, N., Shapiro, A. I., Carone, L., et al. 2025, *ApJL*, 989, L6, doi: [10.3847/2041-8213/adf0fb](https://doi.org/10.3847/2041-8213/adf0fb)
- Kostogryz, N. M., Shapiro, A. I., Witzke, V., et al. 2024, *Nature Astronomy*, 8, 929, doi: [10.1038/s41550-024-02252-5](https://doi.org/10.1038/s41550-024-02252-5)
- Lim, O., Benneke, B., Doyon, R., et al. 2023, *ApJL*, 955, L22, doi: [10.3847/2041-8213/acf7c4](https://doi.org/10.3847/2041-8213/acf7c4)
- Mansfield, M., Bean, J. L., Oklopčić, A., et al. 2018, *ApJL*, 868, L34, doi: [10.3847/2041-8213/aaf166](https://doi.org/10.3847/2041-8213/aaf166)
- McCullough, P. R., Crouzet, N., Deming, D., & Madhusudhan, N. 2014, *ApJ*, 791, 55, doi: [10.1088/0004-637X/791/1/55](https://doi.org/10.1088/0004-637X/791/1/55)
- McQuillan, A., Mazeh, T., & Aigrain, S. 2014, *ApJS*, 211, 24, doi: [10.1088/0067-0049/211/2/24](https://doi.org/10.1088/0067-0049/211/2/24)
- Moran, S. E., Stevenson, K. B., Sing, D. K., et al. 2023, *ApJL*, 948, L11, doi: [10.3847/2041-8213/accb9c](https://doi.org/10.3847/2041-8213/accb9c)
- Morris, B. M., Curtis, J. L., Sakari, C., Hawley, S. L., & Agol, E. 2019, *AJ*, 158, 101, doi: [10.3847/1538-3881/ab2e04](https://doi.org/10.3847/1538-3881/ab2e04)
- Morris, B. M., Hebb, L., Davenport, J. R. A., Rohn, G., & Hawley, S. L. 2017a, *ApJ*, 846, 99, doi: [10.3847/1538-4357/aa8555](https://doi.org/10.3847/1538-4357/aa8555)
- Morris, B. M., Hebb, L., Hawley, S. L., Jones, K., & Romney, J. 2025, *ApJ*, 990, 113, doi: [10.3847/1538-4357/adeca5](https://doi.org/10.3847/1538-4357/adeca5)
- Morris, B. M., Hawley, S. L., Hebb, L., et al. 2017b, *ApJ*, 848, 58, doi: [10.3847/1538-4357/aa8cca](https://doi.org/10.3847/1538-4357/aa8cca)
- Murray, C. A., & Berta-Thompson, Z. 2025, arXiv e-prints, arXiv:2511.03045, doi: [10.48550/arXiv.2511.03045](https://doi.org/10.48550/arXiv.2511.03045)
- Narrett, I. S., Rackham, B. V., & de Wit, J. 2024, *AJ*, 167, 107, doi: [10.3847/1538-3881/ad1f6c](https://doi.org/10.3847/1538-3881/ad1f6c)
- Piaulet-Ghorayeb, C., Benneke, B., Radica, M., et al. 2024, *ApJL*, 974, L10, doi: [10.3847/2041-8213/ad6f00](https://doi.org/10.3847/2041-8213/ad6f00)
- Pinhas, A., Rackham, B. V., Madhusudhan, N., & Apai, D. 2018, *MNRAS*, 480, 5314, doi: [10.1093/mnras/sty2209](https://doi.org/10.1093/mnras/sty2209)
- Pont, F., Knutson, H., Gilliland, R. L., Moutou, C., & Charbonneau, D. 2008, *MNRAS*, 385, 109, doi: [10.1111/j.1365-2966.2008.12852.x](https://doi.org/10.1111/j.1365-2966.2008.12852.x)
- Quintana, E. V., Dotson, J. L., Colón, K. D., et al. 2024, in *Society of Photo-Optical Instrumentation Engineers (SPIE) Conference Series*, Vol. 13092, *Space Telescopes and Instrumentation 2024: Optical, Infrared, and Millimeter Wave*, ed. L. E. Coyle, S. Matsuura, & M. D. Perrin, 1309214, doi: [10.1117/12.3020633](https://doi.org/10.1117/12.3020633)
- Rackham, B., Espinoza, N., Apai, D., et al. 2017, *ApJ*, 834, 151, doi: [10.3847/1538-4357/aa4f6c](https://doi.org/10.3847/1538-4357/aa4f6c)
- Rackham, B. V. 2023, *speclib*, 0.0-beta.0, Zenodo, doi: [10.5281/zenodo.7868050](https://doi.org/10.5281/zenodo.7868050)
- Rackham, B. V., Apai, D., & Giampapa, M. S. 2018, *ApJ*, 853, 122, doi: [10.3847/1538-4357/aaa08c](https://doi.org/10.3847/1538-4357/aaa08c)
- . 2019, *AJ*, 157, 96, doi: [10.3847/1538-3881/aaf892](https://doi.org/10.3847/1538-3881/aaf892)
- Rackham, B. V., & de Wit, J. 2024, *AJ*, 168, 82, doi: [10.3847/1538-3881/ad5833](https://doi.org/10.3847/1538-3881/ad5833)
- Rackham, B. V., Espinoza, N., Berdyugina, S. V., et al. 2023, *RAS Techniques and Instruments*, 2, 148, doi: [10.1093/rasti/rzad009](https://doi.org/10.1093/rasti/rzad009)
- Rackham, B. V., Iyer, A. R., Apai, D., et al. 2026, arXiv e-prints, arXiv:2603.04519, <https://arxiv.org/abs/2603.04519>
- Radica, M., Piaulet-Ghorayeb, C., Taylor, J., et al. 2025, *ApJL*, 979, L5, doi: [10.3847/2041-8213/ada381](https://doi.org/10.3847/2041-8213/ada381)
- Rathcke, A. D., Buchhave, L. A., Wit, J. d., et al. 2025, *ApJL*, 979, L19, doi: [10.3847/2041-8213/ada5c7](https://doi.org/10.3847/2041-8213/ada5c7)
- Rayner, J. T., Toomey, D. W., Onaka, P. M., et al. 2003, *PASP*, 115, 362, doi: [10.1086/367745](https://doi.org/10.1086/367745)

- Ricker, G. R., Winn, J. N., Vanderspek, R., et al. 2015, *Journal of Astronomical Telescopes, Instruments, and Systems*, 1, 014003, doi: [10.1117/1.JATIS.1.1.014003](https://doi.org/10.1117/1.JATIS.1.1.014003)
- Rotman, Y., McGill, P., Welbanks, L., et al. 2026, arXiv e-prints, arXiv:2603.04488, doi: [10.48550/arXiv.2603.04488](https://doi.org/10.48550/arXiv.2603.04488)
- Sanchis-Ojeda, R., & Winn, J. N. 2011, *ApJ*, 743, 61, doi: [10.1088/0004-637X/743/1/61](https://doi.org/10.1088/0004-637X/743/1/61)
- Schutte, M. C., Hebb, L., Wisniewski, J. P., et al. 2023, *AJ*, 166, 92, doi: [10.3847/1538-3881/ace59c](https://doi.org/10.3847/1538-3881/ace59c)
- Shapiro, A. I., Solanki, S. K., Krivova, N. A., et al. 2017, *Nature Astronomy*, 1, 612, doi: [10.1038/s41550-017-0217-y](https://doi.org/10.1038/s41550-017-0217-y)
- . 2014, *A&A*, 569, A38, doi: [10.1051/0004-6361/201323086](https://doi.org/10.1051/0004-6361/201323086)
- Sing, D. K., Pont, F., Aigrain, S., et al. 2011, *MNRAS*, 416, 1443, doi: [10.1111/j.1365-2966.2011.19142.x](https://doi.org/10.1111/j.1365-2966.2011.19142.x)
- Skrutskie, M. F., Cutri, R. M., Stiening, R., et al. 2006, *AJ*, 131, 1163, doi: [10.1086/498708](https://doi.org/10.1086/498708)
- Smitha, H. N., Shapiro, A. I., Witzke, V., et al. 2025, *ApJL*, 978, L13, doi: [10.3847/2041-8213/ad9aaa](https://doi.org/10.3847/2041-8213/ad9aaa)
- Sowmya, K., Shapiro, A. I., Rouppe van der Voort, L. H. M., Krivova, N. A., & Solanki, S. K. 2023, *ApJL*, 956, L10, doi: [10.3847/2041-8213/acf92a](https://doi.org/10.3847/2041-8213/acf92a)
- Speagle, J. S. 2020, *MNRAS*, 493, 3132, doi: [10.1093/mnras/staa278](https://doi.org/10.1093/mnras/staa278)
- Stassun, K. G., Oelkers, R. J., Paegert, M., et al. 2019, *AJ*, 158, 138, doi: [10.3847/1538-3881/ab3467](https://doi.org/10.3847/1538-3881/ab3467)
- Wakeford, H. R., Lewis, N. K., Fowler, J., et al. 2019, *AJ*, 157, 11, doi: [10.3847/1538-3881/aaf04d](https://doi.org/10.3847/1538-3881/aaf04d)
- Wilson, D. J., Froning, C. S., Duvvuri, G. M., et al. 2025, *ApJ*, 978, 85, doi: [10.3847/1538-4357/ad9251](https://doi.org/10.3847/1538-4357/ad9251)
- Yee, S. W., Petigura, E. A., Fulton, B. J., et al. 2018, *AJ*, 155, 255, doi: [10.3847/1538-3881/aabfec](https://doi.org/10.3847/1538-3881/aabfec)
- Zhang, Z., Zhou, Y., Rackham, B. V., & Apai, D. 2018, *AJ*, 156, 178, doi: [10.3847/1538-3881/aade4f](https://doi.org/10.3847/1538-3881/aade4f)
- Zhou, Y., Apai, D., Lew, B. W. P., & Schneider, G. 2017, *AJ*, 153, 243, doi: [10.3847/1538-3881/aa6481](https://doi.org/10.3847/1538-3881/aa6481)
- Zieba, S., & Kreidberg, L. 2022, *The Journal of Open Source Software*, 7, 4838, doi: [10.21105/joss.04838](https://doi.org/10.21105/joss.04838)

APPENDIX

This appendix provides summary tables of the stellar spectral modeling results described in the main text. Table 4 presents the results of the simultaneous retrieval of the WFC3 G102 and G141 spectra. We report posterior medians and credible intervals for the stellar temperatures, filling factors, and nuisance parameters for one-, two-, and three-component models, along with model comparison metrics. Table 5 summarizes the corresponding multi-component fits to the individual STIS (G430L, G750L) and WFC3 (G102, G141) datasets.

Table 4. A retrieval for simultaneous fit of HAT-P-11 with G102 and G141 data.

Param.	Units	Prior	1 Comp	2 Comp	3 Comp
With No Prior					
T_1	K	$\mathcal{U}[2300-6500]$	4779^{+10}_{-10}	4979^{+20}_{-24}	4981^{+26}_{-31}
T_2	K	$\mathcal{U}[2300-6500]$	-	3413^{+77}_{-73}	3402^{+89}_{-88}
T_3	K	$\mathcal{U}[2300-6500]$	-	-	4924^{+167}_{-314}
$f_{1,G102}$		Dirichlet [†]	-	$0.741^{+0.023}_{-0.020}$	$0.667^{+0.052}_{-0.075}$
$f_{2,G102}$		Dirichlet [†]	-	$0.259^{+0.023}_{-0.020}$	$0.253^{+0.026}_{-0.031}$
$f_{3,G102}$	-	Dirichlet [†]	-	-	$0.073^{+0.070}_{-0.050}$
$f_{1,G141}$		Dirichlet [†]	-	$0.669^{+0.046}_{-0.041}$	$0.569^{+0.088}_{-0.101}$
$f_{2,G141}$	-	Dirichlet [†]	-	$0.331^{+0.041}_{-0.046}$	$0.322^{+0.054}_{-0.050}$
$f_{3,G141}$	-	Dirichlet [†]	-	-	$0.105^{+0.095}_{-0.066}$
R_*	R_\odot	$\mathcal{N}(0.760,0.048)$	$0.675^{+0.004}_{-0.004}$	$0.800^{+0.011}_{-0.010}$	$0.797^{+0.011}_{-0.010}$
Fe/H	-	$\mathcal{U}_{[-2,+0.5]}(0.31, 0.05)$	$0.358^{+0.033}_{-0.033}$	$0.344^{+0.030}_{-0.026}$	$0.331^{+0.036}_{-0.035}$
$\ln f_{\text{var}, G102}$	-	$\mathcal{U}[-10-0]$	$-4.982^{+0.055}_{-0.053}$	$-4.709^{+0.068}_{-0.074}$	$-4.722^{+0.073}_{-0.070}$
$\ln f_{\text{var}, G141}$	-	$\mathcal{U}[-10-0]$	$-4.098^{+0.083}_{-0.080}$	$-4.478^{+0.074}_{-0.065}$	$-4.462^{+0.074}_{-0.071}$
a_{G102}	-	$\mathcal{U}[0.5-2]$	$1.253^{+0.008}_{-0.008}$	$0.954^{+0.024}_{-0.023}$	$0.966^{+0.024}_{-0.023}$
a_{G141}	-	$\mathcal{U}[0.5-2]$	$1.224^{+0.009}_{-0.009}$	$1.005^{+0.019}_{-0.018}$	$1.013^{+0.022}_{-0.021}$
ΔBIC	-	-	336.0	✓	16.0
AD Stat.	-	-	0.818	1.198	1.264

NOTE—[†]A Dirichlet prior was used for filling factor such that $f_1 > f_2 > f_3$ and $\Sigma f_i = 1$

Table 5. Multi-components Fits to HAT-P-11 spectra.

Param.	Units	Prior	1 Comp	2 Comp	3 Comp
STIS G430L					
T_1	K	$\mathcal{U}[2300-6500]$	4626 $^{+10}_{-9}$	4625 $^{+17}_{-17}$	4624 $^{+21}_{-20}$
T_2	K	$\mathcal{U}[2300-6500]$	-	4621 $^{+73}_{-116}$	4627 $^{+60}_{-65}$
T_3	K	$\mathcal{U}[2300-6500]$	-	-	4583 $^{+140}_{-462}$
f_1	-	Dirichlet †	-	0.830 $^{+0.148}_{-0.218}$	0.708 $^{+0.186}_{-0.174}$
f_2	-	Dirichlet †	-	0.170 $^{+0.218}_{-0.148}$	0.232 $^{+0.146}_{-0.149}$
f_3	-	Dirichlet †	-	-	0.032 $^{+0.088}_{-0.027}$
R_*	R_\odot	$\mathcal{N}(0.760, 0.048)$	0.793 $^{+0.006}_{-0.006}$	0.793 $^{+0.006}_{-0.006}$	0.794 $^{+0.006}_{-0.006}$
Fe/H	-	$\mathcal{N}_{[-2, +0.5]}(0.31, 0.05)$	0.498 $^{+0.002}_{-0.004}$	0.498 $^{+0.002}_{-0.003}$	0.498 $^{+0.002}_{-0.003}$
$\ln f_{\text{var}}$	-	$\mathcal{U}[-10-0]$	-2.725 $^{+0.043}_{-0.043}$	-2.724 $^{+0.043}_{-0.042}$	-2.724 $^{+0.042}_{-0.042}$
ΔBIC	-	-	✓	20.0	33.0
AD Stat.	-	-	2.641	2.662	2.646
STIS G750L					
T_1	K	$\mathcal{U}[2300-6500]$	4683 $^{+3}_{-3}$	4685 $^{+12}_{-8}$	4701 $^{+16}_{-12}$
T_2	K	$\mathcal{U}[2300-6500]$	-	4662 $^{+63}_{-87}$	4698 $^{+29}_{-27}$
T_3	K	$\mathcal{U}[2300-6500]$	-	-	3044 $^{+146}_{-33}$
f_1	-	Dirichlet †	-	0.879 $^{+0.101}_{-0.201}$	0.684 $^{+0.151}_{-0.141}$
f_2	-	Dirichlet †	-	0.121 $^{+0.201}_{-0.101}$	0.271 $^{+0.134}_{-0.147}$
f_3	-	Dirichlet †	-	-	0.044 $^{+0.020}_{-0.018}$
R_*	R_\odot	$\mathcal{N}(0.760, 0.048)$	0.780 $^{+0.005}_{-0.005}$	0.779 $^{+0.005}_{-0.005}$	0.788 $^{+0.006}_{-0.007}$
Fe/H	-	$\mathcal{N}_{[-2, +0.5]}(0.31, 0.05)$	0.240 $^{+0.021}_{-0.021}$	0.241 $^{+0.020}_{-0.020}$	0.285 $^{+0.034}_{-0.033}$
$\ln f_{\text{var}}$	-	$\mathcal{U}[-10-0]$	-4.301 $^{+0.024}_{-0.024}$	-4.300 $^{+0.023}_{-0.024}$	-4.304 $^{+0.025}_{-0.023}$
ΔBIC	-	-	✓	12.0	25.0
AD Stat.	-	-	2.017	2.004	2.092
WFC3 G102					
T_1	K	$\mathcal{U}[2300-6500]$	4748 $^{+13}_{-13}$	4966 $^{+33}_{-41}$	4975 $^{+35}_{-50}$
T_2	K	$\mathcal{U}[2300-6500]$	-	3617 $^{+125}_{-149}$	3610 $^{+174}_{-188}$
T_3	K	$\mathcal{U}[2300-6500]$	-	-	4407 $^{+549}_{-857}$
f_1	-	Dirichlet †	-	0.736 $^{+0.043}_{-0.038}$	0.684 $^{+0.055}_{-0.097}$
f_2	-	Dirichlet †	-	0.264 $^{+0.038}_{-0.043}$	0.236 $^{+0.048}_{-0.051}$
f_3	-	Dirichlet †	-	-	0.091 $^{+0.074}_{-0.059}$
R_*	R_\odot	$\mathcal{N}(0.760, 0.048)$	0.765 $^{+0.006}_{-0.006}$	0.782 $^{+0.007}_{-0.007}$	0.782 $^{+0.007}_{-0.007}$
Fe/H	-	$\mathcal{N}_{[-2, +0.5]}(0.31, 0.05)$	0.324 $^{+0.044}_{-0.044}$	0.369 $^{+0.041}_{-0.040}$	0.369 $^{+0.041}_{-0.040}$
$\ln f_{\text{var}}$	-	$\mathcal{U}[-10-0]$	-4.599 $^{+0.071}_{-0.069}$	-4.710 $^{+0.069}_{-0.066}$	-4.712 $^{+0.065}_{-0.065}$
ΔBIC	-	-	16.0	✓	10.0
AD Stat.	-	-	1.273	0.793	0.798
WFC3 G141					
T_1	K	$\mathcal{U}[2300-6500]$	4888 $^{+14}_{-15}$	4950 $^{+32}_{-27}$	4961 $^{+41}_{-36}$
T_2	K	$\mathcal{U}[2300-6500]$	-	3326 $^{+110}_{-119}$	3336 $^{+130}_{-130}$
T_3	K	$\mathcal{U}[2300-6500]$	-	-	4623 $^{+495}_{-1291}$
f_1	-	Dirichlet †	-	0.718 $^{+0.051}_{-0.045}$	0.670 $^{+0.056}_{-0.089}$
f_2	-	Dirichlet †	-	0.282 $^{+0.045}_{-0.051}$	0.259 $^{+0.053}_{-0.063}$
f_3	-	Dirichlet †	-	-	0.080 $^{+0.071}_{-0.058}$
R_*	R_\odot	$\mathcal{N}(0.760, 0.048)$	0.730 $^{+0.006}_{-0.006}$	0.802 $^{+0.015}_{-0.016}$	0.803 $^{+0.014}_{-0.014}$
Fe/H	-	$\mathcal{N}_{[-2, +0.5]}(0.31, 0.05)$	0.289 $^{+0.037}_{-0.037}$	0.300 $^{+0.037}_{-0.034}$	0.303 $^{+0.036}_{-0.034}$
$\ln f_{\text{var}}$	-	$\mathcal{U}[-10-0]$	-4.650 $^{+0.079}_{-0.075}$	-4.722 $^{+0.073}_{-0.070}$	-4.749 $^{+0.071}_{-0.070}$
ΔBIC	-	-	22.0	✓	9.0
AD Stat.	-	-	0.416	0.135	0.118

NOTE—The preferred model for each instrument, selected based on the minimum BIC, is shown in bold.

† A Dirichlet prior was used for filling factor such that $f_1 > f_2 > f_3$ and $\Sigma f_i = 1$.